Imbalanced segregation of recombinant haplotypes in hybrid populations reveals inter- and intrachromosomal Dobzhansky-Muller incompatibilities

Juan Li [1,2, 3,#], Molly Schumer[4], Claudia Bank[1,2, 3,#]

1. Institute of Ecology and Evolution, University of Bern, Bern, Switzerland
2. Gulbenkian Science Institute, Oeiras, Portugal
3. Swiss Institute for Bioinformatics, Lausanne, Switzerland
4. Department of Biology, Stanford University, United States

[#]To whom correspondence should be addressed: juan.li@iee.unibe.ch, claudia.bank@iee.unibe.ch

Abstract

Dobzhansky-Muller incompatibilities (DMIs) are a major component of reproductive isolation between species. DMIs imply negative epistasis, exposed when two diverged populations hybridize. Mapping the locations of DMIs has largely relied on classical genetic mapping. Approaches to date are hampered by low power and the challenge of identifying DMI loci on the same chromosome, because strong initial linkage of parental haplotypes weakens statistical tests. Here, we propose new statistics to infer negative epistasis from haplotype frequencies in hybrid populations. When two divergent populations hybridize, the variance of the number of heterozygous sites at two loci decreases faster with time at DMI loci than at random pairs of loci. If two populations hybridize at near-even admixture proportions, the deviation of the observed variance from its expectation becomes negative for the DMI pair. This negative deviation enables us to detect intermediate to strong negative epistasis both within and between chromosomes. The detection window depends on the demographic scenario, the recombination rate, and the strength of epistasis. When the initial proportion of the two parental populations is uneven, only strong DMIs can be detected with our method unless migration prevents parental haplotypes from being lost. We use the new statistics to infer candidate DMIs from three hybrid populations of swordtail fish. We identify numerous new DMI candidates, some of which are inferred to interact with several loci within and between chromosomes. Moreover, we discuss our results in the context of an expected enrichment in intrachromosomal over interchromosomal DMIs.

Author Summary

Genetic incompatibility in the form of (Bateson-)Dobzhansky-Muller incompatibilities (DMIs) is an important component of reproductive isolation between species. However, the evolutionary role of DMIs during the process of speciation is contentious. One step towards addressing this question is to quantify the prevalence of DMIs in incipient and hybridizing species. DMIs occur when two or more genetic variants interact to reduce their carrier's fitness. Once recombination combines incompatible variants in hybrids, selection acts to remove these variants from the population. Here, we present statistics that are sensitive to the resulting recombinant imbalance and that can indicate the location of DMIs in hybrid genomes in various demographic scenarios. We use simulations to show that the time window during which a DMI is detectable depends on its genomic location, the severity of the DMI, and the population's demography. Importantly, our statistic distinguishes genetic associations that arise due to physical linkage

from those arising due to interacting genes, which allows for the inference of both inter- and intrachromosomal DMIs. Applying our statistics to three hybrid populations of swordtail fish, we confirm previous DMIs and identify new candidate incompatibilities.

Introduction

Hybrids between diverged populations often suffer from a fitness disadvantage caused by genetic incompatibilities between two or more loci, called (Bateson-)Dobzhansky-Muller incompatibilities (DMIs). As a result, hybrids may be less fit than their parental species, inviable, or sterile (reviewed in Orr and Presgraves 2000, Fishman and Sweigart 2018). DMIs are common within and between species (Presgraves 2010, Corbett-Detig 2013), often uncovered in crosses between diverged populations or closely related species (reviewed in Wu and Ting 2004, Maheshwari and Barbash 2011).

Despite their biological importance, methods for detecting DMIs in natural hybrid populations tend to have low power and statistical problems. Classical genetic mapping relies on a large sample size of hybrid offspring (i.e., hundreds or thousands of individuals) or exceptionally strong selection and is only designed to detect pairwise interactions. Examples of known hybrid incompatibilities reflect the biases expected from statistical power limited to detecting loci with strong selection against hybrids, e.g., in the case of malignant melanoma that reduce viability in two pairs of *Xiphophorus* species (reviewed in Orr and Presgraves 2000; Powell et al. 2020). In another study, researchers mapped multiple non-independent incompatibilities contributing to male sterility in a house mouse hybrid zone (Turner and Harr 2014).

Another commonly used approach to infer DMIs from hybrid genomes is to search for unexpected statistical associations (linkage disequilibrium; LD) between physically unlinked regions of the genome. Studies of DMIs that use LD signals between physically unlinked loci (interchromosomal DMIs) have taken advantage of data from simulations and experiments (e.g., *Arabidopsis thaliana*, Simon et al. 2008, and yeast, Li et al. 2013, *Drosophila melanogaster,* Corbett-Detig et al. 2013), and genomic data from hybrid populations (e.g., swordtail fish, Schumer et al. 2014, Schumer and Brandvain 2016). Unfortunately, LD-based methods are vulnerable to high false positive rates as a function of hybrid population demographic history, especially ongoing gene flow from source populations (Schumer and Brandvain 2016, Satokangas et al. 2020). Moreover, LD-based statistics are not well suited for detecting interacting loci within chromosomes (intrachromosomal DMIs) in the absence of highly accurate recombination maps. To detect intrachromosomal interactions with LD-based methods, researchers would need to know the exact recombination rates between loci before they could distinguish expected LD caused by physical linkage from excess LD caused by DMIs. The authors of this study are not aware of any existing method that infers both inter- and intrachromosomal DMIs from hybrid genomic data.

Although intrachromosomal DMIs have not been well-studied in the hybrid incompatibility literature, several lines of evidence suggest that they are at least as common as interchromosomal DMIs. First, from a mechanistic perspective, gene order is not random in the genome. Genes tend to cluster on the same chromosome when they are co-expressed, co-regulated, included in the same pathway, or part of a protein-protein complex (reviewed in Hurst 2004). When sequencing and protein precipitation technology (high-C, micro-C) were combined to profile the physical interactions (e.g., interactions mediated by enhancers, insulators, cohesion binding sites, etc.) between DNA sequences, researchers found that most of the interactions were intrachromosomal, manifesting as chromosome territories and topological associated domains (reviewed in Szabo et al. 2019). This genomic architecture of gene regulation

suggests that DMIs within chromosomes are more common than DMIs between chromosomes from first principles.

Second, from an evolutionary perspective, natural selection may favor reduced recombination between loci that are under divergent selection or involved in epistatic interactions (reviewed in Ortiz-Barrientos et al. 2016). Introgression is more common in high recombination rate regions of the genome where linkage disequilibrium breaks down rapidly over physical distance (Brandvain et al. 2014, Schumer et al. 2018, Martin et al. 2019, Chaturvedi 2020). One potential consequence is that high recombination rates disassociate incompatible loci more quickly, whereas tight linkage may facilitate speciation in the face of gene flow (gene coupling, e.g., Bay et al. 2017, Byers et al. 2020; inversions, e.g., Noor et al. 2001). In line with this argument, theoretical studies indicated that hybrid populations isolated from their parent populations are most likely to develop into isolated species (homoploid hybrid speciation) with intermediate recombination rates between DMI loci (Blanckaert and Bank 2018). Given the predicted importance of genome organization in adaptation and speciation, tools to identify intrachromosomal DMIs are needed to understand the architecture of reproductive isolation between species.

Here, we present a new statistical approach to close this key knowledge gap and to infer both inter- and intrachromosomal DMIs. We report that the imbalanced haplotype frequencies caused by selection against DMIs can lead to a unique pattern of LD and heterozygosity. We capture these patterns in two statistics that we name $X(2)$ and $\Delta D2$. We show that sensitivity and specificity of detecting DMIs are high in a range of demographic scenarios and apply our statistics to infer candidate DMIs in three swordtail fish hybrid populations. Based on this analysis, we find that putative DMIs are widespread and complex across hybrid populations of swordtail fish.

Results

Reduced variance in two-locus heterozygosity indicates DMIs

Heterozygosity is the expectation of the number of heterozygous loci per individual across n loci, K, where $K \in [0, 1, 2 \ldots n]$. The variance in n-locus heterozygosity in this study is the variance of K, which can be used to describe the overall extent of linkage disequilibrium (reviewed in Slatkin 2008). In the presence of population structure, the normalized deviation of the variance of K at n loci from its expected value under panmixia and neutrality, $X(n)$, is elevated (Sved 1968, Brown et al. 1980, Maynard Smith et al. 1993, see Methods). That is because with population structure, individuals breed locally, which increases the proportion of groups of homozygous individuals while maintaining polymorphism globally. This, in turn, increases the variance of heterozygosity as compared to the panmictic expectation. Here, we demonstrate that a pairwise DMI, where $n=2$, changes $X(2)$ at DMI loci to negative values in a hybrid population, i.e., it creates a lower-than-expected variance in two-locus heterozygosity. Importantly, this statistic distinguishes LD that occurs due to physical linkage from the specific association of alleles that is caused by selection against a DMI.

To first understand the dynamics of $X(2)$ in the simplest scenario without having to consider dominance of direct selection and epistasis, we used a haploid toy model of a DMI with recombination (Kimura 1965, see also Bank et al. 2012). Consider a haploid panmictic population with two biallelic loci, **A** and **B,** with alleles *a*, *A*, and *b*, *B*, where *aB* and *Ab* represent the parental haplotypes and a hybrid incompatibility exists between alleles *A* and *B*. We follow the haplotype frequency dynamics in a model

with discrete non-overlapping generations, ignoring genetic drift and assuming that recombination occurs with probability c. We denote the fitness of the haplotypes by $w_{ab} = 1, w_{Ab} = 1 + \alpha,\ w_{aB} = 1 + \beta,\ w_{AB} = (1+\alpha)(1+\beta)(1+\gamma)$ (Figure S1). Throughout the paper, we assume that α and β are small positive numbers, representing a weak beneficial effect of A and B (following Blanckaert and Bank 2018), and that $-\gamma \gg \alpha, \beta$ (the incompatibility is much stronger than directional selection). We use this toy model to analyze the dynamics of $X(2)$ and $D2_{ik}$ (defined below) upon formation of a new hybrid population composed of a fraction f of aB parental individuals and a fraction of $1-f$ of Ab parental individuals (i.e., f denotes the initial admixture proportion).

The toy model highlights unique features of haplotype frequency dynamics in new hybrid populations in the presence of a DMI (see also Blanckaert and Bank 2018 for the corresponding diploid model). Recombinant haplotypes ab and AB appear from the second generation onwards. At first, their frequency sharply increases (Figure S2) due to recombination. Then strong selection against the incompatibility sets in that depletes the AB haplotype and gives the ab haplotype a marginal advantage because offspring of ab individuals never harbor the incompatibility (Figure S2). Thus, the strong incompatibility drives haplotype frequency dynamics after recombinants appear.

The two-locus heterozygosity is defined as the sum of heterozygosity over two loci, $h_{\mathbf{A}} + h_{\mathbf{B}}$, where $h_{\mathbf{A}} = 1 - {p_a}^2 - {p_A}^2,\ h_{\mathbf{B}} = 1 - {p_b}^2 - {p_B}^2$ (Nei and Roychoudhury 1974). The expected variance in two-locus heterozygosity is $h_{\mathbf{A}} + h_{\mathbf{B}} - {h_{\mathbf{A}}}^2 - {h_{\mathbf{B}}}^2$ assuming binomial sampling (see Methods). The deviation of the variance in two-locus heterozygosity from its expectation under linkage equilibrium in this model is $\Delta_{var} = 2\sum_i \sum_k ({g_{ik}}^2 - {p_i}^2{p_k}^2)$, where p_j denotes the frequency of allele j and g_{ik} denotes the frequency of haplotype ik, and where we define $D2_{ik} := {g_{ik}}^2 - {p_i}^2{p_k}^2$ for $i \in \{a, A\}, k \in \{b, B\}$ (see Methods). The normalized version of Δ_{var} is $X(2) = \Delta_{var}/exp(Var)$. In a newly-formed panmictic hybrid population, $X(2)$ is initially positive because of the overrepresentation of parental haplotypes as compared with recombinants. Importantly, $X(2)$ becomes negative if the haplotype frequencies are imbalanced, for example if a lethal DMI causes absence of one recombinant haplotype and overrepresentation of the other. Focusing on the two possible recombinants in the scenario described above, this imbalance is captured by $\Delta D2 = D2_{AB} - D2_{ab}$.

The deviation of the variance in two-locus heterozygosity, Δ_{var}, can also be expressed as $\Delta_{var} = 4D(2g_{ab} + 2g_{AB} - 2D - 1)$, where $D = g_{AB}g_{ab} - g_{aB}g_{Ab}$ and $D < 0$ until the population reaches linkage equilibrium or loses the polymorphism at one of the two loci. To fulfill $\Delta_{var} < 0$, the condition $2g_{ab} + 2g_{AB} - 2D - 1 > 0$ must be met, which implies $g_{ab} + g_{AB} - D > \frac{1}{2}$ & $D < 0$. It follows that the frequencies of four haplotypes must be $g_{ab} > g_{aB}, g_{Ab} > g_{AB}$ (Figure S3), indicating haplotype AB is the most unfit haplotype.

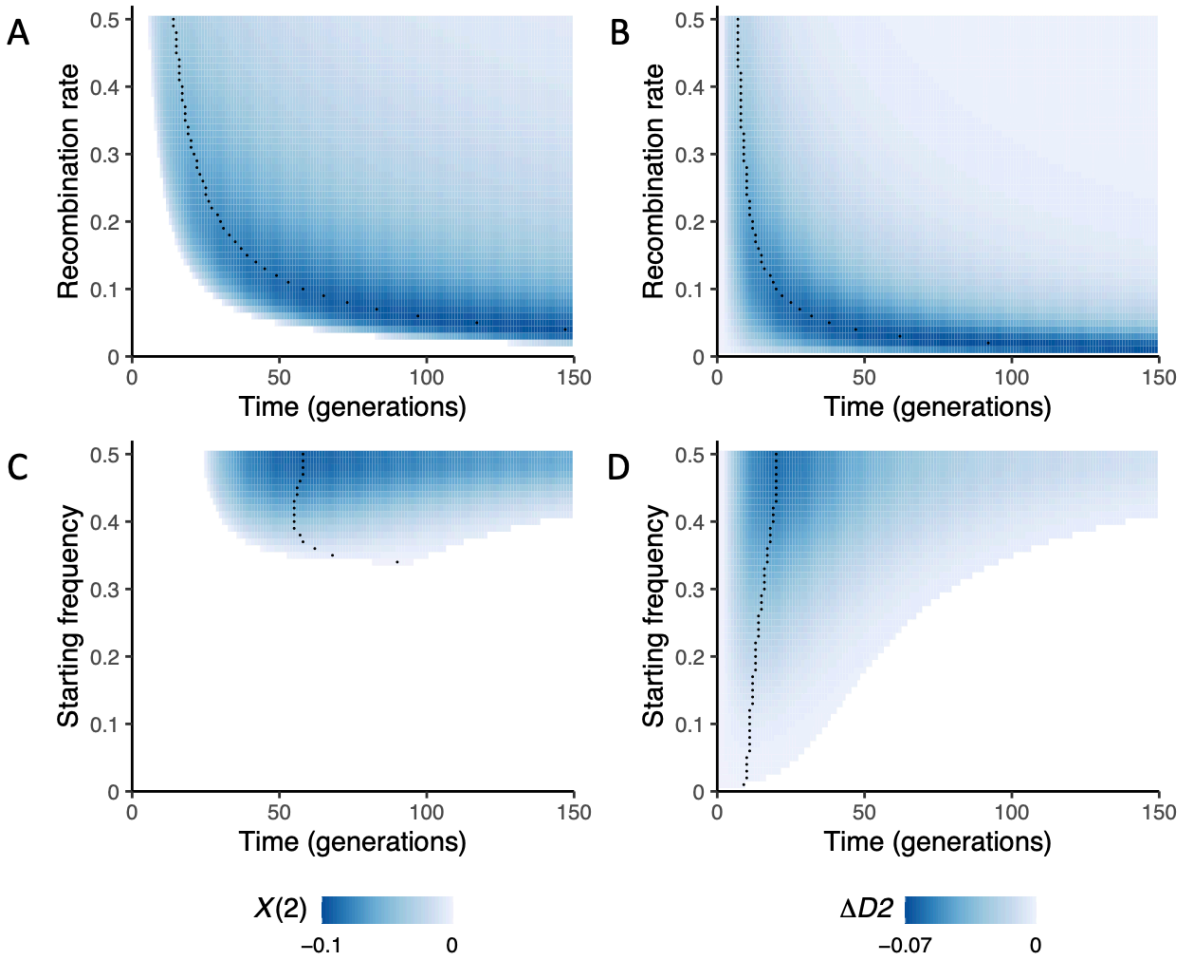

Figure 1. Dynamics of $X(2)$ and $\Delta D2 = D2_{ab} - D2_{AB}$ in the deterministic haploid toy model for different recombination rates and admixture proportions. The model parameters are $\alpha = 0.001, \beta = 0.002, \gamma = -0.5$. Black dots indicate the time with the largest $-X(2)$ or -$\Delta D2$ (i.e., strongest DMI signal) in each trajectory. The values of $X(2)$ and $\Delta D2$ are represented by blue color intensity. Blank areas represent either $X(2)$>0 (to the left of the blue area) or at least one locus close to fixation (minor allele frequency <0.005, to the right of the blue area). A&B. Both $X(2)$ and $\Delta D2$ show more extreme values at intermediate recombination rates. Here, we assumed equal admixture proportions. C&D. Negative $X(2)$ and negative $\Delta D2$ show larger values when admixture proportions are more even. In these two panels, the recombination probability between the two DMI loci is 0.1.

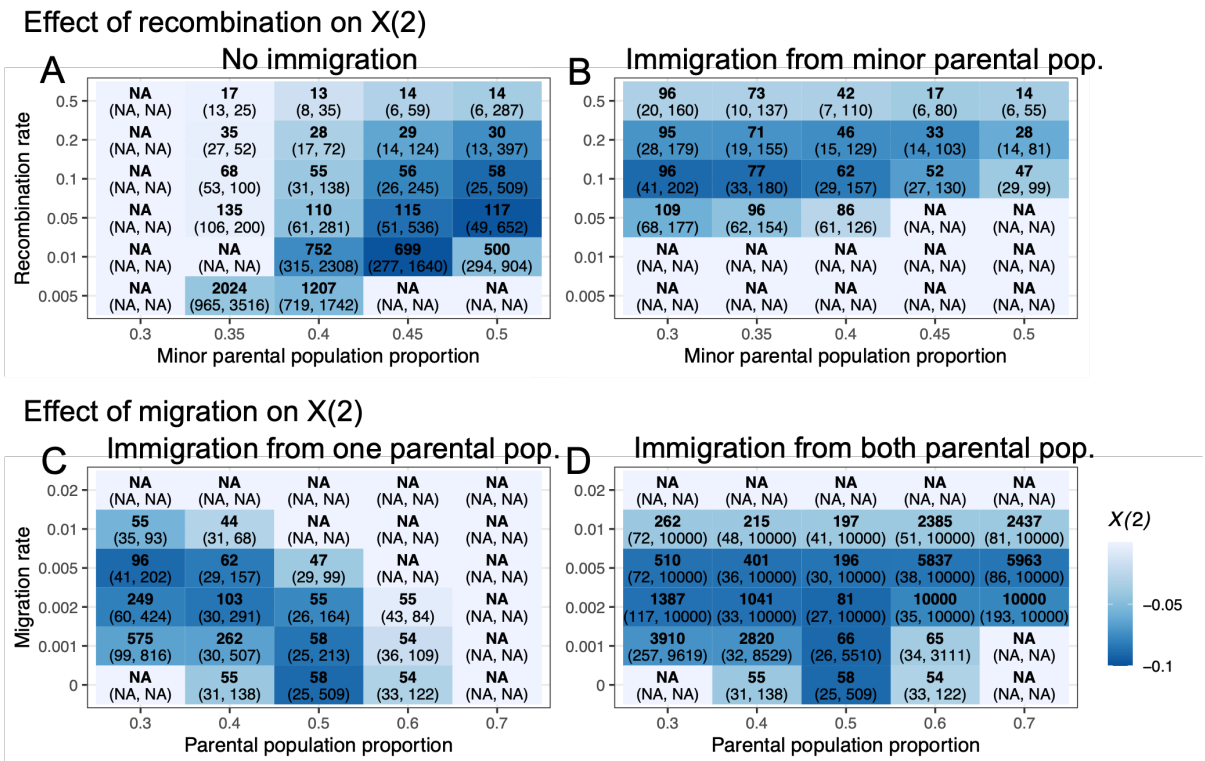

Figure 2. The time window of negative $X(2)$ for a DMI in the deterministic toy model. Generations with the largest $-X(2)$ values are indicated in bold. Time windows for which $X(2)$ is negative for a DMI pair are shown in parentheses. Values of the largest $-X(2)$ observed over that interval are represented by blue color intensity. The model parameters used here are α= 0.001, β = 0.002, γ = -0.5. All trajectories were traced until one locus was near monomorphic (minor allele frequency <0.005 or up to 10000 generations). We considered two parameter sets. One is a range of admixture proportions (x axis) and recombination rates (y axis) without immigration (A) or with immigration from the minor parental population ($m = 0.005$, B). A. The DMI left the strongest signal in $X(2)$ for intermediate recombination rates, and the signal was not detected until later generations when recombination rates were lower and admixture proportions were more uneven. B. Immigration from the parental population can widen the detection window. The other parameter set is a range of admixture proportion (x axis) and immigration (y axis) from one (asymmetric, C) or both parental populations (symmetric, D) when the recombination probability is 0.1. C. Immigration from one parental population can narrow or widen the detection windows. D. Immigration from both parental populations could persist long-term DMIs. Note that the observed asymmetry in D stems from the effect of direct selection.

Unique dynamics of $-X(2)$ at DMI loci

We compared the dynamics of the $X(2)$ statistic at DMI loci in scenarios where the strength of epistasis was strong ($\gamma = -0.5$) relative to scenarios without epistasis (i.e., $\gamma = 0$). Without epistasis and with weak direct selection for A and B ($\alpha = 0.001, \beta = 0.002$), both the recombinant frequencies and their $D2_{ik}$ values are expected to be similar and independent of the admixture proportion, because recombinants are generated at equal proportions and because weak directional selection cannot drive significant imbalance in the recombinant haplotypes (Figure S4 A&B). Conversely, with a strong DMI, segregation of the two recombinants is imbalanced, as is evident from the $D2_{ik}$ trajectories of the two

recombinants (Figure S4 C&D). Interestingly, without epistasis, $X(2)$ rapidly decreases and converges to zero over time (Figure S4 E&F). At equal admixture proportions, $X(2)$ for a DMI rapidly decreases to negative values and then slowly increases over time, reaching 0 when one of the interacting alleles is lost from the population. At intermediate recombination rates, $X(2)$ for a strongly selected DMI ($\gamma = -0.5$) attains its minimal value after around 60 generations (Figure S4 E). In populations in which admixture proportions are highly skewed, negative $X(2)$ values are never observed, even when DMIs are under strong selection (Figure S4 F). One exception to this observation is when the admixture asymmetry is counteracted by immigration from the minor parental population (discussed below). Overall, a DMI causes negative $X(2)$ once the recombinant imbalance due to selection against the DMI overcomes the residual linkage of parental haplotypes.

The signal of negative $X(2)$ generated by selection against a DMI is most pronounced when the admixture proportions are even. In addition, -$X(2)$ and -$\Delta D2$ reach the largest values at low and intermediate recombination rates (Figure 1 A&B). At the same time, the lower the recombination rate between the interacting loci, the longer it takes for recombinants to emerge, resulting in a later appearance of negative $X(2)$ (Figure 2). In theory, this phenomenon suggests that a DMI at any possible recombination distance will be eventually detectable with our approach. An exception is when two loci have vanishingly small recombination probabilities, such that direct selection and genetic drift undermine the signal of the DMI in $X(2)$, because the DMI is purged from the population (by losing one of the interacting partners) before detectable epistasis-induced recombinant imbalance appears. In practice, variation in recombination probabilities will change the time period during which a DMI can be detected.

Regardless of the recombination rate, our toy model suggests that detecting a DMI in an isolated hybrid population using $X(2)$ requires the initial admixture proportion to be near 0.5 (Figure 1 C&D, minor parental frequency 0.3-0.5). Intuitively, this is because the recombinant imbalance $\Delta D2$ (which is $D \cdot (g_{ab} - g_{AB} + p_a p_b - p_A p_B) \propto D \cdot (\gamma - \alpha\beta)$) reaches its largest value at equal admixture proportions since $D = g_{AB} \cdot g_{ab} - g_{aB} \cdot g_{aB}$ is most extreme when $g_{Ab} = g_{aB} = 0.5$. As the recombinant imbalance becomes extreme, $-X(2)$ becomes larger.

We were interested in evaluating whether $-X(2)$ is diagnostic of epistatic selection or sensitive to selection in general. Without epistasis, only strong selection in the same direction acting on both *A* and *B* can generate recombinant imbalance by means of Hill-Robertson interference (Hill and Robertson 1966, Felsenstein 1974). To evaluate the dynamics of $-X(2)$ in this scenario, we assumed that *A* and *B* are under strong negative selection and combine additively, such that haplotype *AB* is the least fit (but without epistasis). Also here, recombinant imbalance results from selection differences between *AB* and *ab* (Figure S1), which cause negative $X(2)$ (Figure S5C) and $\Delta D2$. However, even with strong selection $X(2)$ remains negative only for a few generations at the very early stage of hybridization (before generation 10, Figure S5C). With a DMI, negative $X(2)$ persists for much longer. The stronger the DMI (i.e., the larger the epistasis parameter γ), the larger $-X(2)$ is observed (after generation 10, Figure 2 and S5A). Altogether, non-epistatic strong selection results in less extreme values of $-X(2)$ and $\Delta D2$ that occur – and fade – much earlier than in the presence of a DMI (Figure S5).

Migration can narrow or widen the detection window

Depending on the specific demographic scenario, we find that migration from one or both parental populations can increase the time during which $X(2)$ indicates a DMI (Figure 2). If the minor parental population contributes most migrants, incompatible haplotypes will be continually formed by recombination between resident and immigrant types. Therefore, the DMI persists in the hybrid population for a longer time period, which makes it possible to use $X(2)$ to detect DMIs in scenarios of uneven admixture proportions (Figure 2 A&B). We note that immigration of the major parental population, in turn, reduces our ability to detect a DMI (Figure 2C). When immigration occurs from both parental populations, the recombinant imbalance can remain in the population for a very long time (Figure 2D). Here, depending on the parameters, a migration-DMI-drift balance can be reached which would essentially make the DMI detectable for as long as the demographic scenario persists.

In simulated data $-X(2)$ robustly indicates intra- and interchromosomal DMIs

To demonstrate that detection of intrachromosomal DMIs in genomic data is feasible, we used simulations with SLiM (Haller and Messer 2019, Figure 3). Throughout this paper, we implemented "recessive" DMIs in our model by assuming that individuals that carry a single copy of two incompatible alleles do not suffer from reduced fitness. We simulated evolution of a chromosome in a hybrid population of 5000 individuals that is generated by a pulse of admixture between two parental populations at equal frequencies. Two interacting loci generating a DMI were located at 10 centimorgan (cM) and 20 cM such that the recombination probability between the two loci was 0.1. For these parameters, the deterministic trajectory indicated that a DMI should be detectable within a time window that spanned from generation 25 to 509, with the strongest signal (i.e., largest $-X(2)$) at generation 58 (Figure 2A). Figure 3 shows the distribution of normalized *D,* a commonly used measure of linkage disequilibrium, (D', see Methods), $X(2)$ and $\Delta D2$ at generation 50. At generation 50, parental linkage has mostly broken down between pairs of distant loci, resulting in a peak at $D' = 0$. $D' \neq 0$ only within small genetic distances (Figure 3 A&D). Moreover, the distribution of $X(2)$ across all pairs of loci along the simulated chromosome has decreased to near 0 by generation 50 (resulting in a peak of $X(2)$ at 0, Figure 3B). In general, negative LD ($D = g_{ab} \cdot g_{AB} - g_{Ab} \cdot g_{aB}$) correlates with positive $X(2)$ (Figure 3C). However, the selected pair of loci can be pinpointed by scanning for negative $X(2)$. Negative D' is also observed between the DMI loci (Figure 3D&E). Importantly, whereas the D' signal is consistent with increased LD – that may stem from residual linkage, population structure, or epistatic interaction (Figure 3D) – -$X(2)$ is specifically associated with unexpected recombinant imbalance ($\Delta D2$) caused by the DMI (Figure 3E&F). Interchromosomal DMIs show a similar pattern (Figure S6). As predicted by the toy model (Figure 1 & 2), interchromosomal DMIs show the recombinant imbalance earlier than intrachromosomal DMIs (Figure 2 and S6).

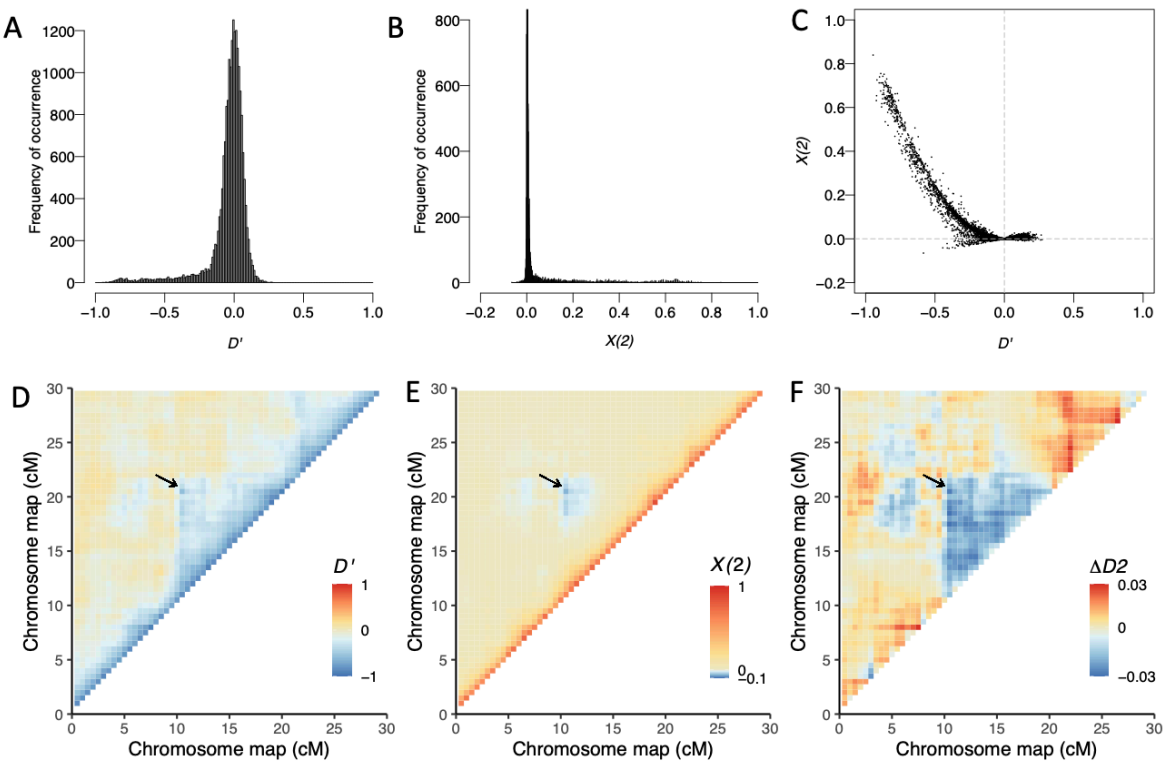

Figure 3. Negative $X(2)$ pinpoints an intrachromosomal DMI in simulated data. The distribution of $X(2)$, D', and $\Delta D2$ of a chromosome with a DMI pair at generation 50 under a Wright-Fisher model for one simulation run using SLiM. The direct selection coefficients are $\alpha = 0.001, \beta = 0.002$. The strength of epistasis is $\gamma = -0.5$. The interacting loci generating the DMI are located at 10 cM and 20 cM, such that the recombination probability is $c = 0.1$ between the two loci. A-C. The distribution of $X(2)$ and D' and their joint distribution within the chromosome. We observe negative $X(2)$ values and negative D' values at the two loci involved in the DMI and in flanking regions that are tightly linked to the DMI. D-F. Heatmaps of D', $X(2)$ and the $\Delta D2$ within the simulated chromosome. Only the DMI region and its 10 cM flanking regions are shown in D-F. The DMI is highlighted by a black arrow.

Since other metrics used to detect DMIs are sensitive to demographic parameters, we next used SLiM to explore whether the same was true for $X(2)$. We first considered the effect of variable population size. Negative $X(2)$ values still appear when the hybrid population size is as small as 300 (Figure 4A). At smaller population sizes, genetic variation in the hybrid population is lost more quickly than for larger populations, which leads to faster purging of the DMIs and thus shortens the detection window (Figure 4A). We further considered the effect of two demographic factors, population expansion and migration, on the sensitivity of the $X(2)$ statistic to DMIs. Natural hybrid populations may suffer from low fertility and high mortality in the early stages of hybridization, and the hybrid population may occupy a new niche or geographical area. As hybrid incompatibilities are purged, mean population fitness increases and the population may expand. To explore the possible effects of this phenomenon, we performed simulations assuming that the hybrid population would expand within 35 generations and arbitrarily defining a 5% growth rate per generation. We found that population expansion rarely affects the detection of a DMI (Figure 4B) since it does not affect the relative genotype frequency dynamics.

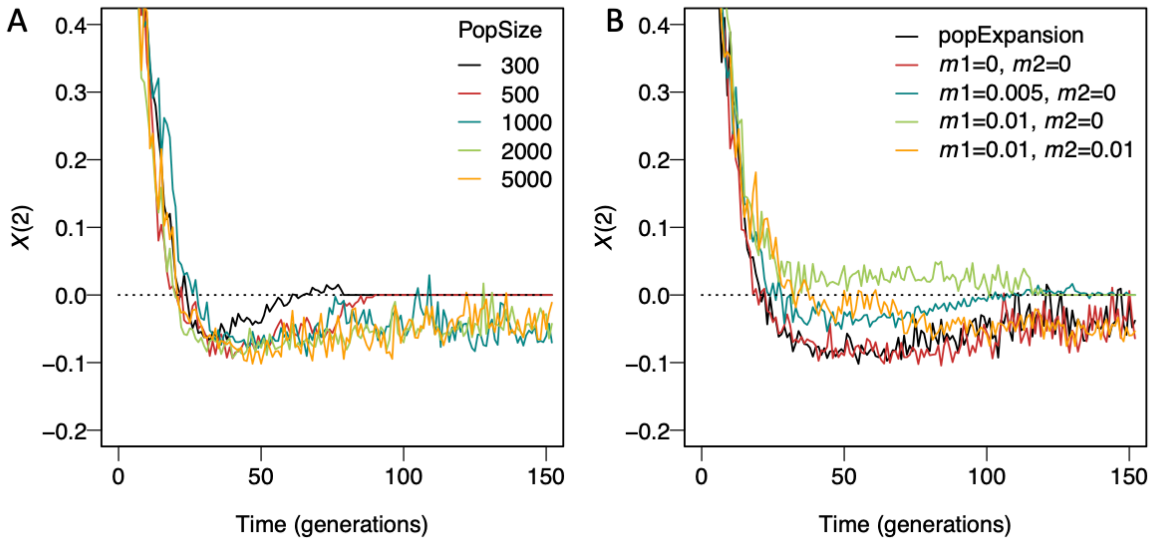

Figure 4. Effect of demographic parameters on the dynamics of $X(2)$ for a DMI in a hybrid population. Each line is one randomly chosen simulation run using SLiM, assuming equal admixture proportions of the parental populations and a strong DMI ($\alpha = 0.001, \beta = 0.002,\ \gamma = -0.5$) under a Wright-Fisher model. The recombination probability between the interacting loci was 0.1. 300 individuals were sampled in each simulation independent of the population size. Individuals that contained <10% of their genome from either parental population were excluded. Trajectories were plotted from generation 2 onwards. A. $X(2)$ dynamics with variable population size. $X(2)$ indicates DMIs when the population size is as small as 300. DMIs are purged more quickly from small populations due to genetic drift. B. $X(2)$ dynamics with population expansion and migration. Immigration rates are $m1$ amd $m2$ from two parental populations. The $X(2)$ signal is only mildly affected by population expansion, low asymmetric migration, and symmetric migration from parental populations. Strong migration from one parental population disrupts DMI detection by $X(2)$ (green curve).

We next considered continual immigration from the parental species into the hybrid population. As shown in Figure 4B, high migration rates initially reduce our ability to detect negative $X(2)$ when admixture proportions are even. However, depending on the specific migration scenario, migration can aid the detection of a DMI. Generally, migration changes the haplotype frequencies and alters the time period during which $X(2)$ is negative (Figure 4B). To quantify this effect, we studied three migration rates, no ($m = 0$), intermediate ($m = 0.005$), and strong ($m = 0.01$) migration from the minor parental population into the hybrid population, and strong migration from both parental populations under even admixture proportions. If the asymmetric migration rate is small to intermediate ($m < 0.005$) or migration rates from two parental populations are symmetric, our simulations suggest that migration does not impede the occurrence of negative $X(2)$ in the presence of a DMI (Figure 2C, 2D and 4B). Symmetric high migration rates could sustain long-term DMIs (Figure 2D and S7).

With strong migration ($m \geq 0.005$), the linkage of parental haplotypes remains strong due to the continuous reintroduction of these haplotypes (Figure S8). In such a scenario, $X(2)$ remains larger than 0

for an extended time. Thus, DMIs can only be detected with $X(2)$ at a later age of the hybrid population, if the DMI alleles have not been purged from the population due to asymmetry of admixture or immigration (Figure 4B & S8). Here, strong migration acts like strong selection for the immigrating parental two-locus haplotypes, which hides the (still existing) recombinant imbalance.

Next, to evaluate the performance of $-X(2)$ in a natural population with overlapping generations, we compared our results from Wright-Fisher simulations with those obtained under a Moran model. With overlapping generations, the emergence of negative $X(2)$ is delayed because recombinant imbalance builds up more slowly than in a model with non-overlapping generations (Figure S9A). At the same time, alleles A and B segregate in the population for much longer with overlapping generations than with non-overlapping generations (Figure S9B). This leads to a longer maintenance time of the interacting loci, resulting in a longer window in which $-X(2)$ can be used to detect the DMI.

Given these results, we next evaluated the sensitivity and specificity of $X(2)$ for DMI detection under a range of models using non-overlapping generations (Figure 5). We simulated four chromosomes, two of which contained the DMI loci and two of which evolved neutrally. We computed sensitivity as the proportion of simulations in which the DMI loci showed $\mathrm{X}(2) < -0.005$ & $D' < 0$, and specificity as one minus the proportion of simulations in which a pair of loci on the neutral chromosomes showed $X(2) < -0.005$ & $D' < 0$. We considered six scenarios by combining two admixture proportions ($f = 0.5$ and $f = 0.3$) and three immigration rates (0, 0.005, 0.01) of the minor parental population. We also compared the performance of $X(2)$ to the G test which has previously been used to detect DMIs (Li and Zhang 2013). The recombination probability in these simulations was set to $c = 0.5$ because the G test can only be applied to unlinked loci.

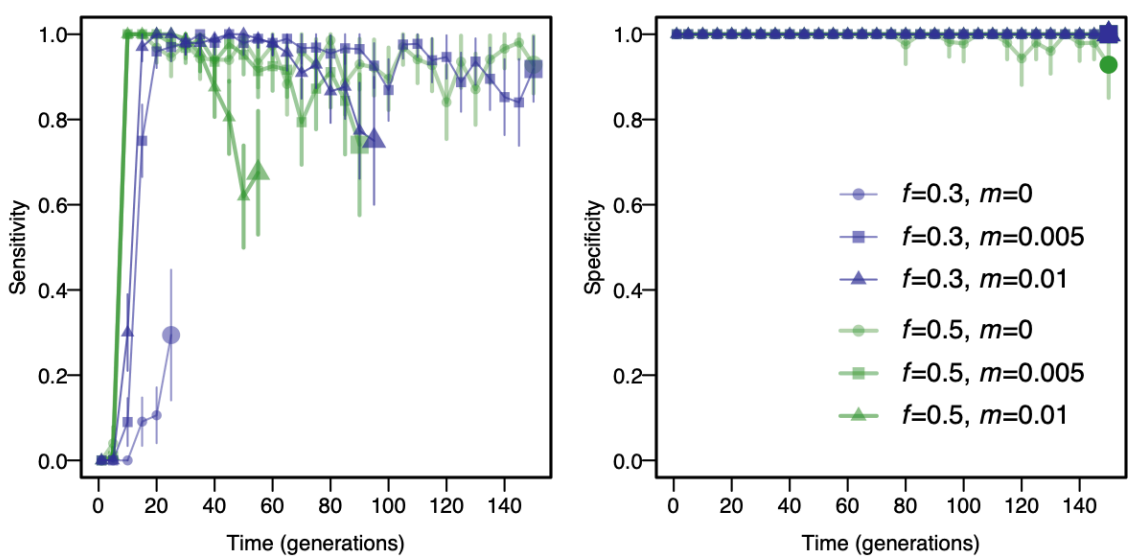

Figure 5. Sensitivity and specificity of negative $X(2)$ for detecting a DMI, computed from 100 simulations of each parameter combination using SLiM, assuming a Wright-Fisher population of 5000 individuals. We considered two admixture proportions, $f = 0.5$ and $f = 0.3$, and three migration rates from the minor parental population: 0, 0.01, and 0.05. A strong DMI ($\alpha = 0.001, \beta = 0.002, \gamma = -0.5$) and no DMI ($\alpha = 0.001, \beta = 0.002,\ \gamma = 0$) were simulated under a Wright-Fisher model. The

recombination probability between the DMI loci was $c = 0.5$. To exclude sampling noise, any interaction with $X(2) < -0.005$ & $D' < 0$ was taken as a putative DMI. Trajectories ended when one of the interacting loci became monomorphic (indicated by large plot markers). Three hundred individuals were sampled in each simulation. A. Sensitivity is high unless strong migration leads to swamping of the DMI alleles. B. Specificity is high under all tested scenarios when no DMI locus is present on the sampled chromosome. Vertical lines represent the 95% confidence interval (Wald test).

In simulations of hybrid populations with non-overlapping generations, equal admixture proportions, and no or moderate levels of ongoing migration from the minor parental population, $X(2)$ allows for detection of the DMI with high sensitivity and specificity (Figure 5, $f = 0.5$, $m = 0$ or 0.005). At high migration rates ($m = 0.01$), migration from the parental population dominates the haplotype frequency dynamics and the DMI cannot be detected with equal admixture proportions. In contrast, immigration can maintain the minor parental alleles when the admixture proportions are uneven ($f = 0.3$). With continuous input of the minor parental haplotype, the DMI remains in the population for longer, so the DMI can be detected based on negative $X(2)$ values until one of the parental haplotypes is lost. Thus, $X(2)$ can be used to detect DMIs in the case of uneven admixture proportions and intermediate migration rates, when immigration counteracts selection against the DMI in the minor parental population. In all scenarios explored here, $X(2)$ has very high specificity. In 300 simulations of a null model of neutral evolution, $X(2)$ was always greater than -0.001, where negative $X(2)$ was caused by genetic drift and random sampling of 300 individuals for the analysis. At low recombination rates, a similar pattern can be observed (Figure S10).

We compared the performance of $X(2)$ with that of the G test, which was identified as one of the best statistics to detect interchromosomal DMIs (Li and Zhang 2013). Figure S11 shows that the G test is highly sensitive in the early stages of hybridization, but its sensitivity decreases after generation 20. There is also an apparent tradeoff between sensitivity and specificity. Interestingly, unlike for the G test there is no tradeoff between sensitivity and specificity for $X(2)$. We found that whereas significant hits using the G test had negative $X(2)$, the opposite was not true, especially when the parental linkage has broken down from generation 20 onwards (Figure 5, S11 and S12). Thus, $X(2)$ was sensitive to DMIs in scenarios in which the G test was not.

Our analysis above relies on the use of phased genotyping data, which can be difficult to collect in practice and can introduce inaccuracies via phasing errors. In contrast, pseudo-phased data are available for many datasets, including the data analyzed below. In this case, only homozygous loci in each genome are used for analyses where the phase can be inferred without computational phasing (e.g., genotyping data reviewed in Davey et al. 2011). We calculated the sensitivity and specificity for the G test and $X(2)$ using only homozygous genotypes (same ancestry state at an ancestry informative site, see methods). The performance for pseudo-phased data trends were similar to phased data with mildly increased sensitivities of $X(2)$ and decreased sensitivities of G test (Figure 5, S11 and S13).

We next applied our detection method to simulated genomic data from a range of more general scenarios with one and two standard DMIs, and a three-locus interaction in which two DMIs have one shared interaction partner. Here, positions of the interacting loci were distributed randomly across four chromosomes (resulting in both inter- and intrachromosomal DMIs), epistatic coefficients were drawn from a uniform distribution ($\gamma \in [-1, -0.001]$), and the direct selection coefficients α and β were drawn

from an exponential distribution with mean 0.001. We further simulated two neutral chromosomes without DMI loci.

On neutral chromosomes, negative $X(2)$ values were always larger than -0.025 (Figure 6A). On chromosomes with DMIs, >75% of negative $X(2)$ were larger than -0.005 (Figure 6B). However, $X(2)$ values can take smaller values up to -0.12 at and close to DMI loci ($-log(X(2))$ close to 1, Figure 6B). $X(2)$ at DMI loci tends to show extreme values (Figure 6C). Notably, under the same selection and demographic parameters, when two DMIs share one locus (three-locus two-DMI model, see Methods), the $X(2)$ distribution at the DMI loci is slightly closer to zero than the distributions for two separate DMIs (Figure 6 and S14). In all cases, $X(2)$ distributions in both models can clearly separate DMI loci from neutral loci (Figure 6 and S14). This indicates that $X(2)$ can still detect DMIs when interaction hubs are present. When only homozygous loci (pseudo-phased data) were used for the inference (Figure S14), the distribution of $X(2)$ values was similar but both the chromosomes with DMIs showed more extreme values. This is because the reduction in sampling size due to pseudo-phasing stochastically results in extremely low numbers or absence of incompatible haplotypes.

The proportion of pairs of loci that were incorrectly inferred as interacting partners (from here on referred to as false positive rate) varied significantly between chromosomes with DMIs and neutral chromosomes (Table S1-S3). For the neutral chromosomes, this proportion was almost 0 when $X(2) < -0.005$ was used as a threshold (Table S2 and S3) for both phased and pseudo-phased data. However, on chromosomes with DMIs, upwards of 2% of pairwise comparisons (from a total of $\binom{400}{2} = 79800$ pairs, of which 2 pairs are true DMI pairs, corresponding to 0.005% of pairs) were identified as putative DMIs based on the $X(2)$ statistic (threshold $X(2) < -0.005$) although the two loci were not involved in a DMI. Most of this signal came from loci in the direct vicinity of the DMI. As expected, both true and false positive rates on the chromosomes with DMIs decreased with a more stringent $X(2)$ threshold (Table S1-S3). Comparing to simulations with a single DMI, the false positive rate increased noticeably but not excessively when two DMIs were simulated (from ~1% to a maximum of 2.2% when $X(2) < -0.005$, Table S1 and S2), indicating some interference between DMIs. When only homozygous loci (pseudo-phased data) were used for the inference, the true positive rate remained similar, but the false positive rate was elevated to 3.6-6.1%, presumably due to stochastic absence of haplotypes due to small sample sizes (Table S2 and S3).

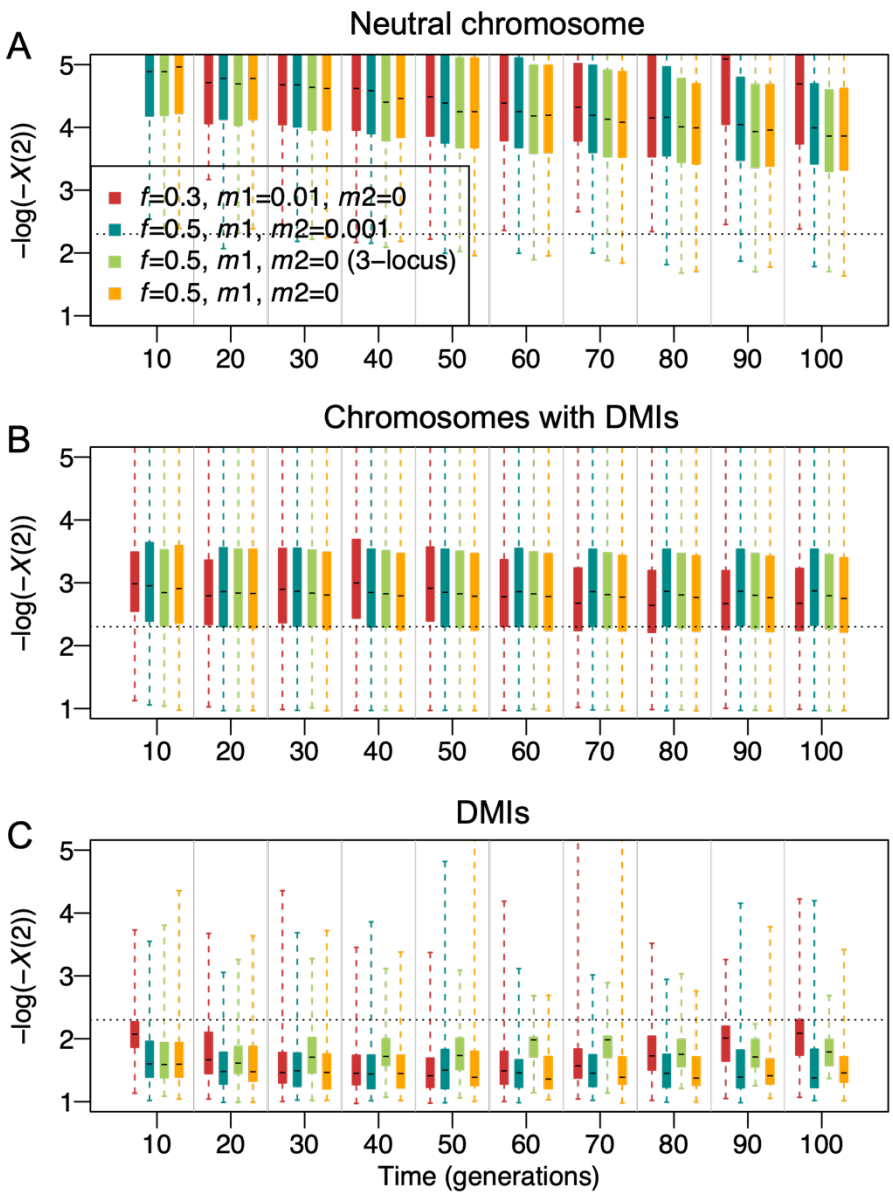

Figure 6. Distributions of negative $X(2)$ when $D' < 0$ for DMI detection under four demographic scenarios. This figure represents two starting frequencies of the minor parental population, $f = 0.5$ and $f = 0.3$, and different immigration rates from the two parental populations ($m1$ from minor parental population, $m2$ from major parental population). Light green boxes show $X(2)$ distribution for the three-locus two-DMI model (3-locus) and the other boxes for the four-locus two-DMI model. DMIs are randomly distributed on four chromosomes. Direct selection coefficients on two incompatible alleles were drawn from an exponential distribution with mean = 0.001. Epistatic coefficients were drawn from a uniform distribution (-1, -0.001); for the three-locus two-DMI model. We calculate $X(2)$ statistics from a sample of two hundred individuals for each simulation. We simulated each scenario 100 times with SLiM. $X(2)$ were summarized at three types of genomic regions, neutral chromosomes (A), chromosomes with DMIs (B), and individual DMI loci (C). Boxplots represent the interquartile range; whiskers extend to minimal and maximal values. The dash line is $X(2) = -0.005$.

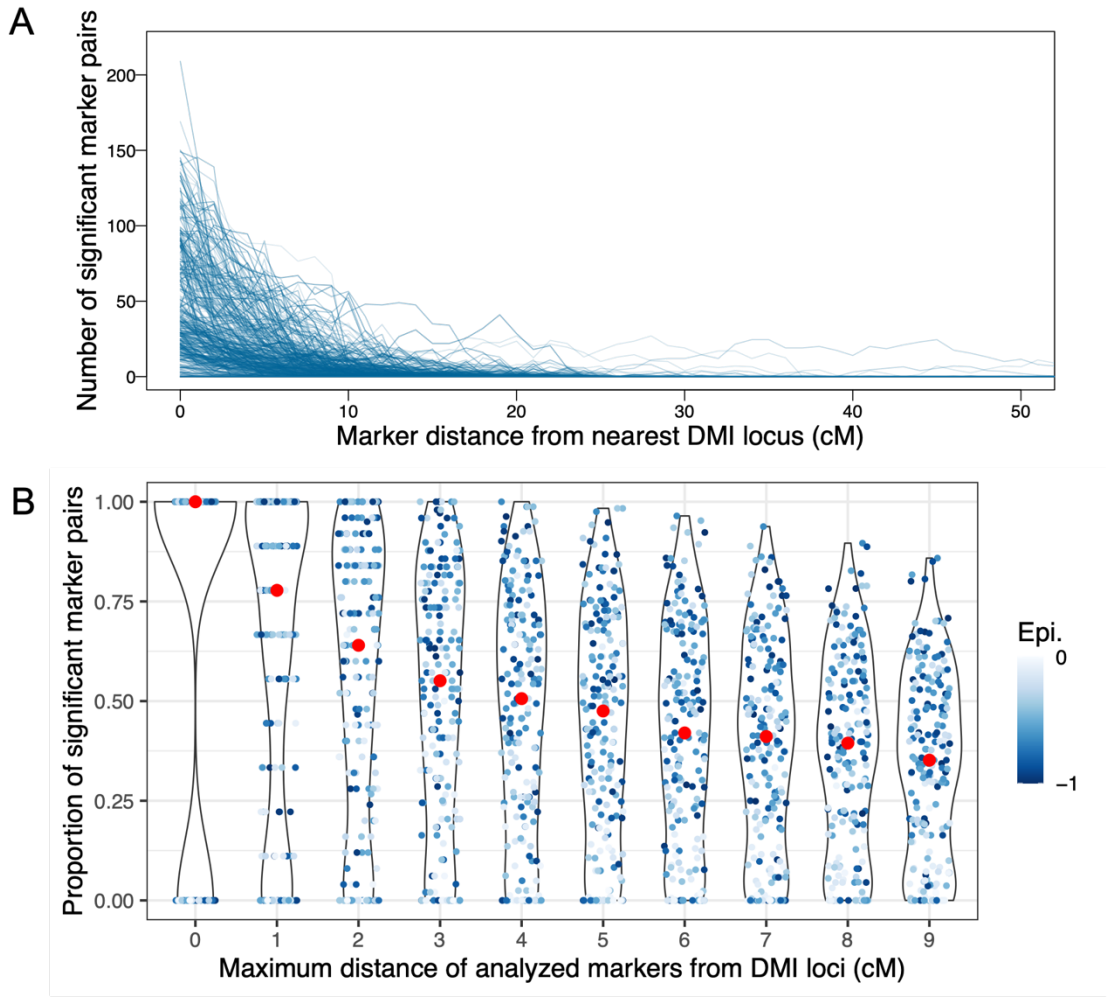

Figure 7. Propagation of the DMI signal into flanking regions in simulated data (sampled at generation 30, significance threshold: $X(2) < -0.005$ & $D' < 0$). Data resulted from 100 simulations using SLiM, in which two DMIs (i.e., four DMI loci) were randomly distributed on four chromosomes, thus resulting in inter- and intrachromosomal DMIs. The direct selection coefficients α and β were drawn from an exponential distribution with mean = 0.001. The strength of epistasis was drawn from a uniform distribution, $\gamma \in$ [-1, -0.001], which are represented by the blue color intensity in panel B. To resemble the demography of the studied hybrid swordtail fish populations, the admixture proportion was set to $f = 0.3$ and the migration rate was $m = 0.01$. Two hundred individuals were sampled from each simulation to obtain the statistics. A. The number of significant marker pairs decreases rapidly with distance to the nearest true DMI locus. B. Proportion of significant marker pairs when statistics were computed for all pairs between two increasingly large regions around the true interacting DMI loci. Red dots indicate the median obtained from 100 simulations. Both weak and strong DMIs can be detected, but weak DMIs tend to leave a weaker signal that did not extend as far as the signal of strong DMIs.

The great majority of false positives was caused by loci linked to DMIs (e.g., Figure 3E and S6). Markers within 10 cM of DMI loci showed a large number of significant $X(2)$ pairs in simulations of two DMIs that were distributed randomly across four chromosomes (Figure 7A). In the most extreme case observed in the simulations, one DMI locus was involved in significant pairwise interactions with over 200 markers of a total of 400 markers (Figure 7A). This case involved strong epistasis for both DMI pairs ($\gamma \approx$

445 -0.75), and two DMI loci that were located very close to each other on the same chromosome (DMI 1
446 between chromosome 1 (chr1) position 63 and chr4 position 100; DMI 2 between chr3 position 98 and
447 chr4 position 92, with the extreme signal emitted from chr3 position 98). Thus, the extreme signal was
448 likely caused by interference between the two DMIs, i.e., a distortion of the signal of one DMI due to
449 selection against the other one. At generation 30, the interaction signal of the two DMIs extends along a
450 large genomic window. Here, the proportion of significant pairs is high within 10 cM of the true DMI loci
451 (median ~35% vs. genomic median 1.1%, Figure 7B and Table S2), probably caused by hitchhiking or
452 limited sorting of large genomic blocks in the young hybrid populations.

453 In analyses of unphased genomic data, we can only rely on information from homozygous genotypes.
454 Therefore, we computed the same statistics for simulated data when only homozygous genotypes were
455 considered (Figure S15). Here, consistent with the lack of resolution suggested above, the proportion of
456 significant pairs between DMI regions decreased more slowly with window size than when the complete
457 data were considered (Figure S15C; see also Figure 7B). We then tested the approach with the strict
458 filtering criteria below to the genomic data from natural hybrid populations before analysis (see below
459 and Methods), for which a homozygous frequency of >0.05 and a frequency of heterozygotes <0.6 were
460 required. Because most strong DMIs are (nearly) purged by generation 30, few DMI loci pass the
461 filtering, and the signal therefore changes such that the highest proportion of significant pairs is observed
462 for genomic windows that span several cM around the true DMI (Figure S15 B&C). Here, only the
463 flanking regions of strong DMIs (and not the DMI loci themselves) indicate the DMI. The proportion of
464 significant pairs at up to 10cM distance from a true DMI locus is still higher than the genome-wide false
465 positive rate (>35% vs. genomic median up to 7.1%, Figure S15B and Table S3). Taken together, our
466 analysis indicates that, although greater precision could be obtained from phased data, our method can
467 identify selection in pseudo-phased data.

468 ***Using $X(2)$ to detect putative DMIs in swordtail fish hybrid populations***

469 Two sibling species of swordtail fish, *Xiphophorus birchmanni* and *X. malinche*, were reported to
470 hybridize naturally in Mexico (Culumber et al. 2011, Schumer et al. 2014). Since these hybrid
471 populations formed recently and have been studied extensively, they represent an excellent opportunity
472 for using $X(2)$ and $\Delta D2$ to infer DMIs from natural populations. Three hybrid populations called CHAF,
473 TOTO and TLMC were sampled and genotyped in previous work (Table S4). All three hybrid
474 populations are estimated to have formed less than 100 generations ago: CHAF ~45 generations; TOTO
475 ~35 generations; TLMC ~56 generations (Schumer et al. 2014 and Powell et al. 2020). However, these
476 admixture times may be underestimated due to ongoing migration (Schumer et al. 2017, 2018, Powell et
477 al. 2020). The estimated proportion of the genome derived from the minor parental population was ~0.25-
478 0.3. The minor parental species for the CHAF and TLMC populations is *X. birchmanni* and for TOTO it
479 is *X. malinche*. All three hybrid populations are known to experience some level of ongoing migration
480 from one parental population (CHAF, ~5%; TOTO, ~3%; TLMC, <<1%; Schumer et al. 2017 and Powell
481 et al. 2020; Table S4). Under the demographic parameters of these natural populations, we expect that in
482 CHAF and TOTO, immigration from the minor parental population counterbalances the asymmetric
483 admixture proportions such that we can infer DMIs with intermediate sensitivity and high specificity
484 (similar to Figure 2, 5, S10 & S13).

485 We used $X(2)$, $\Delta D2$ and D' to identify putative DMI pairs and to infer the most strongly depleted
486 genotypes in these three populations. To roughly count the DMIs in a fashion that is comparable between
487 populations, we sliced the genome into fragments of 1 Megabase (Mb), which we will refer to as a locus
488 in the following analyses. To increase our confidence in the candidates, we performed bootstrapping to
489 ensure that the locus pair was consistently inferred to have negative $X(2)$ and $D' < 0$ (Table S5, see
490 Methods). The number of inferred DMIs is quite robust to different $X(2)$ criteria (from 0 to -0.015, Table
491 S5). A putative DMI was identified if homozygous markers at this locus showed $X(2) < -0.005$ and
492 $D' < 0$ (see also Methods), based on the observation that neutral and DMI loci can be separated by
493 negative $X(2)$ at -0.005 from simulations (Figure 6 and S14).

494 In total, we detected 2203, 2039 and 1442 putative DMIs in the three hybrid populations CHAF, TLMC
495 and TOTO with false discovery proportion <0.001 (15.2%, 12% and 6% of tests, respectively, Table S5).
496 As highlighted by the simulations in the previous section, these numbers may include many genomic
497 blocks that are close to DMIs but do not themselves carry a DMI locus (Figure 7 and S15, Table S5).
498 Given the moderate false positive rate estimated from the simulations, we view this as a preliminary set of
499 candidate DMIs for further investigation. In each population, 200-400 1Mb bins (out of the total 711 1Mb
500 bins, Table S5) were involved in at least one putative DMI. If the putative DMIs were randomly
501 distributed across the genome, the occurrences of the 1Mb bins would fit a Poisson distribution ($\lambda = 2 \cdot$
502 number of putative DMIs / number of 1Mb bins involved in interactions). In contrast to this expectation,
503 1Mb bins with very small and vast numbers of putative interacting partners were greatly overrepresented
504 among the DMI candidates (One-sample Kolmogorov-Smirnov test, $p < 2.2e-16$, Figure S16, Figure
505 S17). We speculate that the 1Mb bins that appear in many putative DMIs are likely to contain true DMI
506 loci in pairwise or complex DMIs, whereas many of the 1Mb bins that occur only once or twice may be
507 noise caused by the true DMI loci. For example, the noise could stem from negative $X(2)$ between two
508 flanking regions of a DMI pair, which is weak but observable. More than 99.5% of putative DMIs are
509 caused by a small number of 1Mb bins that are each involved in >10 putative DMIs (54 in CHAF, 61 in
510 TLMC and 66 in TOTO). Among these putative DMI hubs, CHAF and TLMC share 8 loci, CHAF and
511 TOTO share 2, and TLMC and TOTO share 2 (Table S6). Altogether, these results suggest that the signal
512 we observe is driven by a small set of loci that are involved in complex DMI interactions in the hybrid
513 population at a time point.

514 Although our overall false positive rate is low, given the large number of tests performed in our
515 evaluation of the real data, we can be most confident in putative DMIs that are detected in multiple
516 populations. Across three hybrid populations we found 17 putative DMI pairs shared between TLMC and
517 CHAF, which are the two populations that have the same minor parental population (*X. birchmanni*) and
518 are therefore expected to share more detectable DMIs (Table S7). There were no shared DMI pairs
519 between TOTO and the two other populations. The overlapping proportions are lower than expected by
520 chance with randomly distributed DMIs per population (binominal test, $p < 0.05$). Among all putative
521 interaction partners, 14 loci were shared by three populations, out of which four were previously
522 identified (Table S8). This set of loci are exciting candidates for future work. Out of all putative
523 interactions identified in the swordtail hybrid populations, about 4% were intrachromosomal (CHAF:
524 81/2203; TLMC: 67/2039; TOTO: 55/1442). Notably, none of the inferred intrachromosomal interactions
525 overlapped between any two populations.

526 The small number of overlapping DMI candidate pairs between the populations most likely results from
527 the individual demography of the hybrid populations. Firstly, as we reported above, the $X(2)$ signal of
528 weaker DMIs and more closely linked DMIs appears later. Therefore, differently aged hybrid populations
529 are not expected to display the same set of detectable DMIs. Secondly, the hybrid populations have
530 different admixture proportions and immigration rates (Table S4). These likely result in different sets and
531 directions of purging of DMIs. For example, Figure S18 shows a putative intrachromosomal DMI in
532 TLMC (between chr20:9M and chr20:10M). In the $\Delta D2$ heat plot of this genomic region, the candidate
533 recombinant from TLMC (composed of *X. birchmanni* ancestry at chr20:9M and *X. malinche* ancestry at
534 chr20:10M) also showed a weak signal of elimination in CHAF. However, in TOTO, which has opposite
535 admixture proportions, no such recombinant imbalance is visible. Another interchromosomal DMI also
536 has a similar pattern in TLMC and CHAF, but with less residual recombinant imbalance in the flanking
537 regions in TOTO, where the focal locus is already fixed (Figure S19).

538 In comparisons between TLMC and CHAF, which share a minor parent species, two loci stood out with
539 respect to their many inferred interaction partners. Both chr20:23Mb (specifically, between 23Mb and
540 23.4Mb) and chr15:15M (specifically, between 15.6Mb and 16Mb) are putatively involved in 8
541 interchromosomal interactions. At both loci, alleles from *X. malinche* are incompatible with alleles at
542 several loci from *X. birchmanni* (Table S7). Interestingly, there was no signal of an interaction between
543 these two loci. However, chr18:19Mb is putatively interacting with both chr20:23Mb and chr15:15Mb in
544 both TLMC and CHAF. *X. malinche* is the major parental population in TLMC and CHAF, leading to the
545 expectation that homozygous *X. malinche* alleles would be in the majority. In contrast to this expectation,
546 few alleles from *X. malinche* remained in these regions when combined with several *X. birchmanni*
547 backgrounds. In TOTO, where *X. malinche* is the minor parental population, many *X. malinche* alleles
548 were already lost from the population or are segregating at very low frequencies. This leads to a power
549 reduction for detecting *X. malinche*-specific interacting partners hinting at why the two strong DMI
550 candidates may not be detectable in TOTO. For example, at locus chr20:23M, frequencies of
551 homozygous *X. malinche* genotypes were found at a median frequency of 0.004, which is much smaller
552 than our filtering criteria 0.05. No DMIs remained detectable in TOTO at locus chr15:15M, at which the
553 frequencies of homozygous *X. malinche* genotypes were found at a median frequency 0.009. Together,
554 our results point at chr20:23Mb and chr15:15Mb as strong DMI candidates at which *X. malinche* alleles
555 are deleterious in combination with certain (and possibly several) loci from *X. birchmanni*.

556 In addition to comparing our candidates with a list of previously identified DMIs (Table S6 and S8), we
557 specifically analyzed genomic regions involved in a well-studied DMI that is known to induce melanoma
558 in hybrids. Powell et al. recently found a DMI between chr5:10-11Mb (*cd97*) and chr21:16.5-17.5Mb
559 (*Xmrk,* Powell et al. 2020). A previous QTL assay predicted that another gene, *cdkn2a/b* (~chr5:16-17Mb;
560 reviewed in Patton et al. 2010) interacted negatively with *Xmrk*. Previous work studying the interaction
561 between *Xmrk* and *cd97* has focused on CHAF, where melanoma frequency is high (interactions
562 generating melanoma appear to have been purged in the other hybrid populations). Interestingly, in
563 CHAF, it appears that both homozygous hybrid haplotypes are depleted in a part of this region. Thus, the
564 *Xmrk-cd97* interaction could be a hybrid incompatibility in which both recombinant haplotypes are
565 deleterious, in which case no negative $X(2)$ signal is expected (since the signal is driven by recombinant
566 imbalance as caused by classical DMIs). Regarding the potential DMI between *Xmrk* and *cdkn2a/b*, we
567 found negative $X(2)$ in at least two hybrid populations that support this interaction (Figure S20, Table
568 S9). In CHAF and TOTO, markers linked to *Xmrk* passed the filtering criteria, but none in TLMC (Table

569 S9). In CHAF, $X(2)$ of 49.5% of marker pairs was negative but only 0.2% of these passed the threshold
570 $X(2) < -0.005$. In TOTO, which is of intermediate age, 25.9% of all marker pairs showed $X(2) <$
571 -0.005, which is much higher than the expectation obtained for a DMI from bootstrapping
572 (median=5.7%, Table S5). This is consistent with our expectation of the signal of an intermediate-strength
573 DMI that does not display strong negative $X(2)$ until later generations.

574 **Discussion**

575 DMIs play an important role in maintaining reproductive isolation between species. Despite their crucial
576 importance, existing methods to identify DMIs are underpowered and susceptible to high false positive
577 rates. Here, we show that the deviation of the variance in two-locus heterozygosity from its expectation,
578 $X(2)$, can allow us to identify intra- and interchromosomal DMIs in hybrid genomes. Specifically, a
579 negative $X(2)$ statistic is indicative of the presence of a DMI, because epistatic selection transiently leads
580 to an imbalance of the recombinant haplotypes. A second measure that we develop, $\Delta D2$, quantifies this
581 recombinant imbalance more explicitly. After showing the expected sensitivity and specificity of these
582 statistics in simulations, we used $X(2)$, $\Delta D2$ and D' to infer candidate DMIs from three hybrid
583 populations of swordtail fish. Although the detection power with these statistics is strongly dependent on
584 the age and demographic history of the hybrid population, false positive rates across simulations of
585 various scenarios were low and are expected to be especially low among interactions detected in multiple
586 populations. Encouraged by this result, we found that natural hybrid populations of swordtail fish
587 harbored many potential DMIs, and our analysis detected known DMI pairs. Interestingly, putative DMI
588 pairs tended to include the same loci more often than expected by chance, which is suggestive of the
589 presence of interaction hubs in these data.

590 ***DMIs cause distinctive patterns of LD and variance in two-locus heterozygosity***

591 Linkage disequilibrium (LD) between physically unlinked loci has been frequently used to identify
592 candidate DMIs. However, LD is influenced by many factors including selection, population structure,
593 population differentiation, genetic drift, and epistasis. Sved first proposed the variance in two-locus
594 heterozygosity as a measure of multi-locus LD (Sved 1968). Generally, LD tends to raise the variance in
595 heterozygosity above its expected value at linkage equilibrium. This deviation from the expectation
596 (called $X(n)$, where n is the number of loci considered) was used to infer population structure within
597 species, e.g., in natural populations of *Hordeum spontaneum* and bacteria (Brown et al. 1980, Maynard
598 Smith et al. 1993). These studies assumed that the focal loci are independent and that any disruption of
599 independence would cause LD and a positive deviation from the expected variance in n-locus
600 heterozygosity (positive $X(n)$). Our study shows that selection against DMIs generates a unique pattern
601 of LD and $X(2)$, where LD is strong but $X(2)$ becomes negative. The conditions for negative $X(2)$ are
602 met when the imbalance happens between a pair of repulsive haplotypes (here, ab and AB) and this pair
603 of haplotypes is in deficiency (linkage disequilibrium, $D = g_{ab} - p_a p_b < 0$).

604 ***DMI inference with $X(2)$ does not rely on recombination rate estimates***

605 One advantage of our statistics is that they do not rely on knowledge of recombination rates, which are
606 often unknown or estimated with error and may also differ between the parental and the hybrid
607 populations. For example, the protein PRDM9 specifies the locations of recombination hotspots in many

608 mammalian species (reviewed in Smukowski and Noor 2011, Penalba and Wolf 2020). Traditional
609 methods of intrachromosomal DMI detection are strongly affected by recombination rate variation,
610 whereas in the case of $X(2)$ it solely affects the temporal scale over which DMIs are detected. At the
611 same time, incorporating recombination rate information into DMI detection with $X(2)$ is an exciting
612 direction for future work. That is because if the recombination map was known, our statistics could be
613 incorporated in a simulation-based framework to estimate not only the location but also the strength of
614 selection against the DMI (i.e., the size of the epistasis coefficient γ).

615 ***Detection time window strongly depends on population demography***

616 The ability to detect a DMI based on negative $X(2)$ and $\Delta D2$ statistics is transient. The time window
617 during which a DMI is detectable with these statistics depends on the demographic history of the
618 population and the strength of the incompatibility and the recombination probability between the two loci
619 involved (Figure 2). Specifically, the less recombination there is between two DMI loci and the weaker
620 the incompatibility, the longer it takes for their recombinant imbalance to be exposed. Moreover, since an
621 intrachromosomal (or weak interchromosomal) DMI is purged more slowly, it is detectable for a longer
622 time period, unless one of the interacting alleles is lost by other forces (such as genetic drift). This
623 interaction between population history and power to detect a DMI must be considered when interpreting
624 $X(2)$ results from real data.

625 Interestingly, certain migration scenarios improve the power to detect DMIs over long time periods. In
626 isolated hybrid populations, DMIs can only be detected within a limited time window, while the DMI loci
627 are still segregating in the population. With the aid of migration from the minor parental population or
628 balanced migration from both parental populations, DMI loci become monomorphic much later.
629 Specifically, continual immigration from both parental populations can maintain both weak and strong
630 DMIs at a steady state in a hybrid population. Negative $X(2)$ could show those segregating DMIs.
631 Considering that LD-based methods are vulnerable to high false positive rates when there is migration
632 from parental populations (Schumer and Brandvain 2016, Satokangas et al. 2020), $X(2)$ could be an
633 excellent addition to DMI detection in such scenarios.

634 Blanckaert and Payseur 2021 discussed the hitchhiking effect that is caused by strong DMIs. Even if DMI
635 loci are already monomorphic or at low frequency beyond the detection limit, linked polymorphic loci
636 could still carry the imbalance signal. Although our study considers this case as a false positive,
637 considering such linked variation could extend the time window for DMI detection.

638 Previous simulations showed that DMIs could only be identified with large sample sizes (800~1600
639 individuals suggested, Li and Zhang 2013). We showed that $X(2)$ can indicate DMIs with sample sizes as
640 low as 200 individuals. In the future, phased data or improved phasing approaches will further improve
641 the power of detecting DMIs with $X(2)$.

642 ***No evidence for enrichment in intrachromosomal DMIs in swordtail population data***

643 Two lines of evidence led us to hypothesize that intrachromosomal DMIs may be overrepresented as
644 compared with interchromosomal DMIs. From first principles, systems and molecular biology have
645 established that genes in the same biological pathway tend to cluster physically in the genome. DMIs may
646 be more likely to arise from disruption or modification of such pathways (reviewed in Hurst 2004). This

647 predicts an enrichment in intrachromosomal DMIs under any scenario of speciation. Secondly,
648 evolutionary theory has predicted that tightly linked DMIs are more likely to accumulate and be
649 maintained in the presence of gene flow (Bank et al. 2012). Thus, both factors should contribute to an
650 enrichment (or reduced purging) of intrachromosomal DMIs. In contrast, in the set of DMI candidates
651 inferred from empirical data in this paper, interchromosomal DMIs were slightly overrepresented as
652 compared to intrachromosomal DMIs (<4% intrachromosomal DMIs compared with the expectation of
653 4.2% given an average chromosome length 29.2 ± 4.63 Mb; permutation test, $p < 0.02$). However, given
654 so many unknowns about the true architecture of selection, we are currently not able to conclude whether
655 this is a biological result, or a pattern caused by the limits of our inference method combined with the
656 demographic history of the populations studied here. Although our method is the first that can be applied
657 to detect intrachromosomal DMIs, it is limited to pairs of loci that are at a sufficiently large distance on
658 the chromosome such that recombination occurs with appreciable frequency, thus making the
659 recombinants visible to selection. Therefore, we are likely to miss local interactions, such as those
660 between neighboring genes. Moreover, intrachromosomal DMIs are detected on a different timescale than
661 interchromosomal DMIs, making the two classes not directly comparable. Altogether, our analysis does
662 not allow for a firm statement about the true proportion of intra- to interchromosomal DMIs.

663 ***The challenge of inferring and understanding complex DMIs***

664 We find based on simulations that our statistics are robust to various demographic scenarios such as
665 population expansions and overlapping generations. However, in the modeling and simulation parts of
666 this paper, we mainly study the dynamics of one or two DMI pairs. This is because considering multiple
667 or complex DMIs would generate an intractably large parameter space to explore. Thus, we implicitly
668 assume that DMIs are independent of other incompatible loci in the genome. However, our results
669 indicate that some DMI candidates are involved in many interactions. For example, one locus may
670 interact with multiple loci (e.g., Brideau et al. 2006, Tang et al. 2015). Moreover, DMIs generate fitness
671 costs in hybrids, but these costs can express themselves through different fitness-related phenotypes. This
672 makes it difficult to study DMIs in the same way one would study a quantitative trait. For example,
673 previous studies suggest that *cdkn2a/b* and *Xmrk* interact in some species of swordtail fish (reviewed in
674 Patton et al. 2010). However, Powell et al. 2020 recently showed that *Xmrk* interacts with a previously
675 unidentified locus (*cd97*) to cause melanoma in other swordtail fish species (Powell et al. 2020). Our
676 results also indicate an interaction between *Xmrk* and a genomic block with *cdkn2a/b* in swordtail fish,
677 which might cause unfit phenotypes other than melanoma. Lu et al. 2020 reported that *rad3d*, a gene
678 upstream of *cdkn2a/b,* interacted with *Xmrk* mapped in hybrids between *X. maculatus* and *X. helleri*.
679 Taken together, this suggests the simultaneous presence of multiple hybrid incompatibilities caused by
680 *Xmrk*. This finding is not specific to this study system; recent GWAS and QTL mapping studies in a
681 house mouse hybrid zone also suggested multiple, non-independent genetic incompatibilities (Turner and
682 Harr 2014, Turner et al. 2014). In addition to the presence of true hubs of hybrid incompatibilities, other
683 types of selection and interference could contribute to the signal at these loci. For example, there could be
684 interference between different DMIs (analogous to Hill-Roberson interference), or strong negative
685 interactions may cause local stratification of the genome (e.g., Pool 2015).

686 Moreover, it is important to note that the sensitivity of the $X(2)$ statistic is specific to the recombinant
687 imbalance caused by classical DMIs (Orr 1995, Gavrilets 1997), where only one recombinant haplotype
688 suffers from the incompatibility, whereas the other has similar fitness to the parental genotype. The

689 evolution of this type of hybrid incompatibility is easy to explain without invoking multi-locus
690 interactions (Orr 1995). However, hybrid populations may carry hybrid incompatibilities beyond classical
691 DMIs, where both recombinant haplotypes suffer from reduced fitness (e.g., Moran et al. 2021). These
692 tend to be less easily purged by gene flow (Bank et al 2012, Lindtke and Buerkle 2015, Blanckaert et al
693 2020), and they may cause distinct patterns in the genome such as inflated single-locus heterozygosity. To
694 date, we are far from understanding the relative prevalence of hybrid incompatibilities of different types
695 and their overall role during hybridization and speciation.

696 According to analysis of hybrid data in swordtail fish, many of the genomic regions analyzed are
697 predicted to be involved in DMIs. While possible, this is likely driven by linkage and analysis choices
698 made for these data. Specifically, based on our simulations, we observe four phenomena that generate
699 negative $X(2)$: true DMI interactions, interaction signals from a flanking region with a DMI locus,
700 interaction signals from two flanking regions and interference between DMIs. However, we suspect that
701 we can be confident in loci which we inferred to be involved in DMIs in multiple populations or
702 interactions. Based on this, we speculate that we may have detected 50-70 loci involved in DMIs per
703 swordtail fish hybrid population. In other species, at least 100 loci were experimentally identified among
704 closely related species (reviewed in Wu and Palopoli 1994, Matute et al. 2010, Moyle and Nakazato 2010,
705 Guerrero et al. 2017). Previous genetic mapping studies and our study of natural hybrid populations have
706 inferred DMIs at the resolution of large genomic blocks. Because speciation genes and genes involved in
707 the same pathway are expected to cluster, the actual number of incompatible genes might be larger than
708 the estimations.

709 ***Concluding remarks***

710 In this paper, we take a step towards genome-wide identification of inter- and intrachromosomal DMIs,
711 providing a powerful new tool for researchers in speciation genetics. However, the complexity of
712 potential interactions in the genotype-fitness map of an organism is vast (Fragata et al. 2019), and DMIs
713 are only one specific kind of pairwise epistatic interaction that is characterized by the fitness deficit of
714 one recombinant genotype. Even if this type of (negative) epistasis between two loci is inferred, drawing
715 conclusions about the functional underpinnings of this epistasis is difficult. For example, Kryazhimskiy
716 (2021) recently presented theoretical models that demonstrate how epistasis can propagate across modules
717 of a metabolic network, with negative epistasis at lower levels possibly resulting in amplified negative
718 epistasis at a higher level, and positive epistasis at a lower level possibly turning into negative epistasis at
719 a higher level. These findings reinforce the expectation of widespread negative epistasis (including DMIs)
720 for fitness. Mapping and functionally understanding complex interactions and their consequences for
721 genome evolution will require new interdisciplinary approaches that combine the tools and expertise from
722 genomics, systems and molecular biology and population genetics in the future.

723 **Materials and methods**

724 ***A toy model illustrates DMI dynamics.***

725 We first consider a toy model of a single DMI pair, similar to Bank et al. 2012, that is purged from an
726 isolated hybrid population. Consider two divergent loci resulting in parental haplotypes *aB* and *Ab*
727 (Figure S1). Hybridization and recombination generate two recombinant haplotypes, *ab* and *AB*. We

assume a DMI between A and B, and that direct selection acts on the incompatible alleles A and B. We denote the fitness of the haplotypes as $w_{ab} = 1, w_{Ab} = 1 + \alpha, w_{aB} = 1 + \beta, w_{AB} = (1 + \alpha)(1 + \beta)(1 + \gamma)$. Throughout the manuscript, we usually set these coefficients to $\alpha = 0.001, \beta = 0.002, \gamma = -0.5$, representing weak direct selection and a strong DMI. To gain an intuition of the purging process and the statistics, we first compare the frequency dynamics with and without DMIs by assuming haploid hybrid populations with recombination in a deterministic model.

Dynamics of the variance in heterozygosity for a two-locus DMI

In the model described above, we denote g_{ik} as the frequency of haplotype ik, where $i \in \{A, a\}$ and $k \in \{B, b\}$. The allele frequency of allele i at locus **A** is p_i, and the allele frequency of allele k at locus **B** is p_k. The heterozygosity h at a locus is $h_{\mathbf{A}} = 1 - {p_a}^2 - {p_A}^2,\ h_{\mathbf{B}} = 1 - {p_b}^2 - {p_B}^2$. The heterozygosity h is the expectation of the number of heterozygous loci per individual across two loci, K, where $K = 0,1,2$. This can be written as the sum of the heterozygosity at **A** and **B** is (Nei and Roychoudhury 1974),

$$h = h_{\mathbf{A}} + h_{\mathbf{B}}.$$

We define the variance of K as in Sved 1968, summing over the contributions of numbers of heterozygous loci (see Table S10), as

$$\begin{aligned}\sigma_{het} &= (0-h)^2\left({g_{Ab}}^2 + {g_{aB}}^2 + {g_{ab}}^2 + {g_{AB}}^2\right) + (1-h)^2(2g_{ab}g_{Ab} + 2g_{ab}g_{aB} + 2g_{AB}g_{Ab} + 2g_{AB}g_{aB}) \\ &\quad + (2-h)^2(2g_{aB}g_{Ab} + 2g_{ab}g_{AB}) \\ &= h_{\mathbf{A}} + h_{\mathbf{B}} - {h_{\mathbf{A}}}^2 - {h_{\mathbf{B}}}^2 \\ &\quad + 2\sum_i\sum_k({g_{ik}}^2 - {p_i}^2{p_k}^2) \\ &= h_{\mathbf{A}} + h_{\mathbf{B}} - {h_{\mathbf{A}}}^2 - {h_{\mathbf{B}}}^2 + 4\sum_i\sum_k p_ip_kD_{ik} + 2\sum_i\sum_k {D_{ik}}^2,\end{aligned}$$

where $D_{ik} = g_{ik} - p_ip_k$ is the LD for each haplotype.

If there is no LD, the alleles that segregate at different loci in an individual are independent, so the expected value of the variance of K is $\sigma_2^{exp} = h_{\mathbf{A}} + h_{\mathbf{B}} - {h_{\mathbf{A}}}^2 - {h_{\mathbf{B}}}^2$.

The deviation of the variance from the independent expectation is therefore

$$\Delta_2 = 4\sum_i\sum_k p_ip_kD_{ik} + 2\sum_i\sum_k {D_{ik}}^2.$$

Its relative deviation from the expectation is

$$X(2) = \frac{\Delta_2}{\sigma_2^{exp}},$$

which is the focal statistic of this paper. Similar to LD, $X(2)$ indicates the association between alleles at two loci. The association is created by recombination, genetic drift, and negative epistasis between alleles.

The LD of recombinants is $D = g_{ab} \cdot g_{AB} - g_{aB} \cdot g_{Ab}$.

Normalizing D to D' we obtain

$$D' = \frac{D}{D_{max}},$$

where

$D_{max} = min(-p_A \cdot p_B, -p_a \cdot p_b)$ when $D < 0$;

$D_{max} = max(p_A \cdot p_b, p_a \cdot p_B)$ when $D > 0$.

We use D' as a classical measure of LD throughout the manuscript.

ΔD2 quantifies imbalanced segregation of recombinant haplotypes

We also rewrote the deviation of the variance of K from its expectation in the form of haplotype frequencies (g_{ik}) and allele frequencies (p_i, p_k)

$$\Delta_2 = 2\sum_i \sum_k ({g_{ik}}^2 - {p_i}^2 {p_k}^2)$$

We propose $D2_{ik} = {g_{ik}}^2 - {p_i}^2 {p_k}^2$ as a measure of the imbalance of haplotype frequencies, which is a key indicator of a DMI.

In a deterministic model without selection, we expect the recombinant haplotypes to be generated at the same frequency after hybridization. It follows that $D2_{ab}$ and $D2_{AB}$ of recombinant haplotypes are expected to be equal initially, independent of the initial admixture proportions. When there is a DMI, the recombinant haplotype *AB* is depleted, and this expectation does not hold. We use the *D2* difference between the two recombinants to refer to DMI-indicating recombinant imbalance and from now on refer to this as $\Delta D2 \coloneqq D2_{AB} - D2_{ab}$ (Figure S4 A-D).

$D2_{ik}$ can also be written as linkage disequilibrium D times a factor, $D2_{ik} = (g_{ik} - p_i p_k)\,(g_{ik} + p_i p_k) = D \cdot (g_{ik} + p_i p_k)$. Therefore, we expect $D2_{ik}$ to be 0 when the population approaches linkage equilibrium (D approaches 0; Figure S4 A-D). The total deviation of $D2_{ik}$ from 0, $\sum_i \sum_k |D2_{ik}|$, is an indicator of linkage disequilibrium. The proportion of $\Delta D2$ over the sum of all $|D_{ik}|$, $(D2_{AB} - D2_{ab}) / \sum_i \sum_k |D2_{ik}|$, can also be written as $|1 - p_A - p_B|$, showing the relationship between the recombinant imbalance and the elimination of the two alleles that interact negatively in the DMI.

Haploid and diploid populations and the dominance of epistasis in our model

Modeling DMIs in a diploid population is more complicated than suggested by the toy model, which assumes a haploid population with recombination. In a diploid population, the epistatic interaction depends on the dominance of each incompatible allele (Table S11). To avoid this complexity, we assumed a haploid population with recombination to demonstrate the dynamics of DMI in a deterministic way with a minimal number of parameters. We can understand the haploid model in a way to assume that selection acts on the gamete pool. Here, heterozygosity is the proportion of heterozygous sites observed when two haplotypes are randomly selected. Figure S21 shows that $X(2)$ trajectories have similar shapes but with different detection time windows ($X(2) < 0$) when a DMI is in either recombining haploid

population or diploid populations with various scenarios of dominance. Because dominant incompatible alleles are exposed to negative epistasis more strongly, higher dominance results in shorter detection windows.

Simulation of a DMI under Wright-Fisher and Moran models

In our simulations, implemented in SLiM (version 3.5, Haller and Messer 2019), we assumed a population size of 5000 diploid individuals, with selection occurring at the juvenile stage, followed by random mating and recombination. For simplicity and computational speed, we ignored mutation (similar to Blanckaert & Bank 2018). At the beginning of the simulation, two fully diverged parental populations of adults are combined at admixture proportions f and $1-f$, which mate randomly. When considering immigration, we assume that migrants from one parental population enter the hybrid population at the juvenile stage after selection. Direct fitness is multiplicative and heterozygous-heterozygous individuals do not suffer from the DMI, similar to the "recessive" DMI scenario in Turelli and Orr 2000 and Blanckaert & Bank 2018, where the DMI affects homozygous-homozygous genotypes ($w_{AB/AB} = (1+\alpha)^2(1+\beta)^2(1+\gamma)^4$) and homozygous-heterozygous genotypes ($w_{AB/aB} = (1+\alpha)(1+\beta)^2(1+\gamma)^2$ and $w_{AB/Ab} = (1+\alpha)^2(1+\beta)(1+\gamma)^2$). Individuals were excluded from sampling if they were nearly purely parental in their ancestry (i.e., <10% of genomes from either parental population).

To represent the demography of the studied swordtail fish populations that have overlapping generations, we compared the DMI dynamics and the difference in the time period in which DMIs can be detected between a non-overlapping generation model (Wright-Fisher) and an overlapping generation model (Moran), both of which operate in discrete time. In the Moran model, mortality rates for each age determined the age structure [0.2, 0.2, 0.0, 0.0, 0.0, 0.0, 0.25, 0.5, 0.75, 1.0] from age 0 to 9 in every generation. Age 0 is the new generation of juveniles. Probability of death for each individual was determined according to these mortality rates and individuals that experienced mortality were replaced by juveniles after selection.

Sensitivity and specificity

Before applying the statistics to real data, we used simulations under a Wright-Fisher model with variable admixture proportions and migration rates to estimate the sensitivity and specificity of our method in detecting DMIs (Figure 2). We designed these simulations to correspond to realistic conditions for its application to swordtail fish data. According to empirical estimates, the migration rate m ranges from <<0.01 to ~0.05 in the natural hybrid populations studied here. To roughly explore these dynamics in our simulations, we included no ($m = 0$), intermediate ($m = 0.005$) and strong ($m = 0.01$) migration from minor parental populations, and two admixture proportions $f \in \{0.3, 0.5\}$. We used the proportion of successful DMI detection under our model to estimate sensitivity, or the true positive rate. Specificity was estimated by the proportion of pairs that were correctly classified not to be DMIs under a null model of neutral evolution. Since $X(2)$ was always larger than -0.001 in the 300 simulations we performed on neutrally evolving pairs, DMI detection criteria were set to $X(2) < -0.005$ & $D' < 0$. $D' < 0$ ensures that the depleted haplotype is a recombinant but not a parental haplotype. The population size was 5000 in each simulation, and the recombination probability was set to 0.5 f or each pair of loci. We simulated

each scenario 100 times and randomly sampled 300 individuals for further analysis. Sensitivity and specificity were calculated from generation 10 onwards. 95% Confidence intervals were estimated using the Wald test (Agresti and Coull 1998).

False and true positive rates with one and two DMI pairs

To generalize the performance analyses, we simulated genomes with one DMI or two DMIs on two or four chromosomes (chromosomes with DMIs are referred to as DMI chromosomes below). In the same genome, two additional neutral chromosomes were simulated to estimate the false positive rate. One hundred markers were simulated on each chromosome, and the population size was set to 5000. The position of the DMI loci were distributed randomly on the DMI chromosomes such that DMIs could be either intra- or interchromosomal. Epistatic coefficients were drawn from a uniform distribution ($\gamma \in [-1, -0.001]$)). Direct selection coefficients were drawn from an exponential distribution (mean=0.001, α, β). Here, the fitness was computed as the product of the respective fitness of the two DMIs. Due to the large parameter space, we only considered three demographic scenarios, equal admixture proportions without migration ($f = 0.5, m1, m2 = 0$), equal admixture proportion with migration from both parental population ($f = 0.5, m1 = m2 = 0.005$) and uneven admixture proportions with high migration rates from the minor parental population ($f = 0.3, m = 0.01$). We simulated each scenario 100 times, such that 100 DMIs in the one-DMI scenario and 200 DMIs in the two-DMI scenario could be used to determine the true positive rates. We also studied the distribution of the total number of retained two-locus haplotypes when only homozygous loci were considered for varying sample sizes ($n \in \{100, 200, 300\}$) in the two-DMI model. At least 200 individuals had to be sampled to obtain >50 homozygous-homozygous haplotypes (Figure S22). The mean and 95% confidence interval of the false positive rate was estimated by resampling 2000 interactions from all pairwise statistics of 100 simulations 1000 times.

To represent interaction hubs, we implemented a three-locus two-DMI model that directly extends the two-locus implementation. Here, two loci (**A** and **B**) are interacting with a third locus (**C**). In our implementation, this results in two pairwise DMIs between alleles A and C, and B and C (Table S12). With multiplicative fitness, haplotype ABC then suffers the lowest fitness in the population. Among the three DMI alleles (A, B and C), allele C on average suffers the lowest fitness because three of the four haplotypes that contain allele C (AbC, aBC, ABC, not abC) are under strong negative epistasis. Allele C would thus be eliminated very quickly in the population. Here, the true and false positive rates are surveyed under equal admixture without migration ($f = 0.5, m = 0$). Five chromosomes were analyzed, including three chromosomes with randomly distributed DMI loci and two neutral chromosomes.

Fish data availability, quality control and bias control

Previous work has described our approach for local ancestry inference in *X. birchmanni* x *X. malinche* hybrids in detail (Powell et al. 2020, Schumer et al. 2020). Ancestry informative sites were defined based on a combination of low and high coverage sequenced individuals from two allopatric *X. birchmanni* (N=150) and two allopatric *X. malinche* populations (N=33). The difference in sequencing effort reflects a large difference in genetic diversity and the expected number of segregating sites between the two species (*X. birchmanni* π per basepair is 0.1%, *X. malinche* is 0.03%). Based on observed allele frequencies at these sites, we excluded any ancestry informative site that had less than a 98% frequency difference between the two samples. We used observed frequencies at these ancestry informative sites, in combination with counts for each allele from low-coverage whole genome sequence data to infer local

872 ancestry using a hidden Markov model (HMM) based approach. The expected performance of this
873 approach was evaluated in simulations, on pure parental individuals not used in the definition of ancestry
874 informative sites and on early generation F_1 and F_2 hybrids where small switches in ancestry can
875 confidently be inferred to be errors. A subset of simulations also included genetic drift between the
876 reference panels and parental populations that form the hybrid populations (Schumer et al. 2020). Based
877 on these analyses we estimated error rates to be ≤0.2% errors per ancestry informative site in all tested
878 scenarios (Powell et al. 2020, Schumer et al. 2020). Thus, given the high expected accuracy of ancestry
879 inference in *X. birchmanni* x *X. malinche* hybrids, we do not expect that errors will cause the patterns
880 observed in the empirical data from natural populations.
881
882 For convenience in downstream analysis, posterior probabilities from the HMM for ancestry state were
883 converted to hard calls. Sites with a posterior probability greater than >0.95 for a particular ancestry state
884 (homozygous *X. malinche*, heterozygous, homozygous *X. birchmanni*) were converted to a hard call for
885 that ancestry state. This resulted in 629112, 629582, and 629101 calls at ancestry informative sites for
886 analysis across populations. Individuals were excluded from this dataset if they were nearly pure parental
887 in their ancestry (i.e., <10% of genomes from either parental population).
888
889 To avoid biases, we filtered ancestry informative sites (makers) in the three populations independently
890 using the same criteria. Here, we defined homozygous genotype when the same ancestry state is at one
891 ancestry informative site in one individual; heterozygous genotype when the different ancestry state is at
892 one ancestry informative site in one individual. In each population, we retained a locus for analysis if its
893 frequency of each homozygous genotype was >0.05, and if the locus was missing (or heterozygous) in
894 fewer than 60% of individuals. Ancestry informative sites were thinned by LD ($r^2 > 0.9$) within a 10kb
895 window, with 1-marker step size by PLINK (v1.9, Chang et al. 2015). The thinning resulted in 18,188,
896 7,244, and 7,415 markers for CHAF, TLMC, TOTO respectively.
897
898 We then sampled 700 markers and calculated the statistics (including $X(2)$, D', $\Delta D2$ and haplotype
899 frequencies) pairwise in this data set. If $X(2) < -0.005$ and $D' < 0$ (Table S1-S3), we considered a pair
900 of markers as a candidate DMI pair. To compare the DMI locations among bootstrap replicates and
901 between hybrid populations, we next split the genome into 1Mb bins (based on the reference genome
902 of *X. maculatus*; Schartl et al. 2013). This window size was inspired by our simulations and two examples
903 in three hybrid populations, which showed that the signal of selection at DMI loci could extend to at least
904 1-2Mb (Figure 3, S6, S18 & S19). Any two bins that contained pairwise interaction candidates were
905 finally considered a putative DMI. We repeated this procedure 20 times.
906
907 The proportion of putative DMIs in all pairwise comparisons was very similar to the expected false
908 positive rate obtained from our simulations, and the proportion of putative DMIs was elevated when
909 markers were assigned to 1Mb bins (Table S3 and S5). To be conservative, given this result, we used
910 several approaches. We used the median proportion p of candidate bins with negative $X(2)$ over 20
911 bootstrap samples as a baseline false positive rate. We then computed the probability of sampling the
912 same candidate interaction between bins (based on choosing different markers in each round) multiple
913 times; this should be binomially distributed with parameter p. Using a binomial test, we determined k as
914 the least number of times that an interaction candidate should be observed to be retained as a putative
915 DMI, using a p value of 0.05 corrected for a false discovery rate of 0.001 (following the Benjamini-

Hochberg procedure). We obtained values of k between 6 and 10 for the three hybrid populations (see Table S5). As a second approach to reduce false positives, we also limited our focus to interactions that were observed in multiple populations. Independent observation of interactions in two or more populations provides strong evidence that these interactions are not expected by chance.

Code availability

All simulation and analysis code that was developed to obtain the results presented in this paper will be deposited in an open archive upon publication of the manuscript and is currently available at https://github.com/banklab/DMI-inference-X2.

Acknowledgments

We are grateful for helpful discussions and comments on the manuscript provided by the IGC-FCUL-unibe journal club and Milan Malinsky. We thank Vitor Sousa for extensive feedback and discussions and Alexandre Blanckaert for simulation code and discussions. We thank Kali Tal for her editorial suggestions. CB and JL are grateful for support by EMBO Installation Grant IG4152 and by ERC Starting Grant 804569 - FIT2GO. CB and MS are grateful for support by the HFSP Young Investor Grant RGY0081/2020. MS is also supported by Sloan, Searle, and Pew fellowships. Calculations were performed on UBELIX (http://www.id.unibe.ch/hpc), the HPC cluster at the University of Bern. This study was greatly improved by insightful comments from two anonymous reviewers and Hilde Schneemann.

References

Bank C, Bürger R, Hermisson J. The limits to parapatric speciation: Dobzhansky–Muller incompatibilities in a continent–island model. Genetics. 2012;191(3):845–863.

Bay RA, Arnegard ME, Conte GL, Best J, Bedford NL, McCann SR, et al. Genetic coupling of female mate choice with polygenic ecological divergence facilitates stickleback speciation. Current Biology. 2017;27(21):3344–3349.

Blanckaert A, Bank C, Hermisson J. The limits to parapatric speciation 3: Evolution of strong reproductive isolation in presence of gene flow despite limited ecological differentiation. Philosophical Transactions of the Royal Society B. 2020;375(1806):20190532.

Blanckaert A, Bank C. In search of the Goldilocks zone for hybrid speciation. PLoS genetics. 2018;14(9): e1007613.

Blanckaert A, Payseur BA. Finding hybrid incompatibilities using genome sequences from hybrid populations. Molecular Biology and Evolution. 2021; 38(10):4616-4627.

Brandvain Y, Kenney AM, Flagel L, Coop G, Sweigart AL. Speciation and introgression between Mimulus nasutus and Mimulus guttatus. PLoS Genet. 2014;10(6): e1004410.

Brideau NJ, Flores HA, Wang J, Maheshwari S, Wang X, Barbash DA. Two Dobzhansky-Muller genes interact to cause hybrid lethality in Drosophila. science. 2006;314(5803):1292–1295.

Brown A, Feldman M, Nevo E. Multilocus structure of natural populations of Hordeum spontaneum. Genetics. 1980;96(2):523–536.

Byers KJ, Darragh K, Fernanda Garza S, Abondano Almeida D, Warren IA, Rastas PM, et al. Clustering of loci controlling species differences in male chemical bouquets of sympatric Heliconius butterflies. Ecology and evolution. 2021;11(1):89–107.

Chang CC, Chow CC, Tellier LC, Vattikuti S, Purcell SM, Lee JJ. Second-generation PLINK: rising to the challenge of larger and richer datasets. Gigascience. 2015;4(1): s13742–015.

Chaturvedi S, Lucas LK, Buerkle CA, Fordyce JA, Forister ML, Nice CC, et al. Recent hybrids recapitulate ancient hybrid outcomes. Nature communications. 2020;11(1):1–15.

Corbett-Detig RB, Zhou J, Clark AG, Hartl DL, Ayroles JF. Genetic incompatibilities are widespread within species. Nature. 2013;504(7478):135–137.

Culumber Z, Fisher H, Tobler M, Mateos M, Barber P, Sorenson M, et al. Replicated hybrid zones of Xiphophorus swordtails along an elevational gradient. Molecular ecology. 2011;20(2):342–356.

Davey JW, Hohenlohe PA, Etter PD, Boone JQ, Catchen JM, Blaxter ML. Genome-wide genetic marker discovery and genotyping using next-generation sequencing. Nature Reviews Genetics. 2011;12(7):499–510.

Felsenstein J. The evolutionary advantage of recombination. Genetics. 1974;78(2):737–756.

Fishman L, Sweigart AL. When two rights make a wrong: the evolutionary genetics of plant hybrid incompatibilities. Annual review of plant biology. 2018; 69:707–731.

Fragata I, Blanckaert A, Louro MAD, Liberles DA, Bank C. Evolution in the light of fitness landscape theory. Trends in ecology & evolution. 2019;34(1):69–82.

Gavrilets S. Hybrid zones with Dobzhansky-type epistatic selection. Evolution. 1997;51(4):1027–1035.

Guerrero RF, Muir CD, Josway S, Moyle LC. Pervasive antagonistic interactions among hybrid incompatibility loci. PLoS genetics. 2017;13(6): e1006817.

Haller BC, Messer PW. SLiM 3: forward genetic simulations beyond the Wright–Fisher model. Molecular biology and evolution. 2019;36(3):632–637.

Hurst LD, Pál C, Lercher MJ. The evolutionary dynamics of eukaryotic gene order. Nature Reviews Genetics. 2004;5(4):299–310.

Kimura M. Attainment of quasi linkage equilibrium when gene frequencies are changing by natural selection. Genetics. 1965;52(5):875.

Kryazhimskiy S. Emergence and propagation of epistasis in metabolic networks. Elife. 2021;10: e60200.

Li C, Wang Z, Zhang J. Toward Genome-Wide Identification of Bateson–Dobzhansky–Muller Incompatibilities in Yeast: A Simulation Study. Genome biology and evolution. 2013;5(7):1261–1272.

984 Lindtke D, Buerkle CA. The genetic architecture of hybrid incompatibilities and their effect on barriers to
985 introgression in secondary contact. Evolution. 2015;69(8):1987–2004.

986 Lu Y, Sandoval A, Voss S, Lai Z, Kneitz S, Boswell W, et al. Oncogenic allelic interaction in
987 Xiphophorus highlights hybrid incompatibility. Proceedings of the National Academy of Sciences.
988 2020;117(47):29786–29794.

989 Maheshwari S, Barbash DA. The genetics of hybrid incompatibilities. Annual review of genetics. 2011;
990 45:331–355.

991 Martin SH, Davey JW, Salazar C, Jiggins CD. Recombination rate variation shapes barriers to
992 introgression across butterfly genomes. PLoS biology. 2019;17(2): e2006288.

993 Matute DR, Butler IA, Turissini DA, Coyne JA. A test of the snowball theory for the rate of evolution of
994 hybrid incompatibilities. Science. 2010;329(5998):1518–1521.

995 Nei M, Roychoudhury AK. Sampling variances of heterozygosity and genetic distance. Genetics.
996 1974;76(2):379–390.

997 Moyle LC, Nakazato T. Hybrid incompatibility "snowballs" between Solanum species. Science.
998 2010;329(5998):1521–1523.

999 Moran BM, Payne CY, Powell DL, Iverson ENK, Banerjee SM, Langdon QK, et al. A Lethal Genetic
1000 Incompatibility between Naturally Hybridizing Species in Mitochondrial Complex I. bioRxiv. 2021;
1001 doi:10.1101/2021.07.13.452279.

1002 Noor MA, Grams KL, Bertucci LA, Reiland J. Chromosomal inversions and the reproductive isolation of
1003 species. Proceedings of the National Academy of Sciences. 2001;98(21):12084–12088.

1004 Orr HA, Presgraves DC. Speciation by postzygotic isolation: forces, genes and molecules. BioEssays.
1005 2000;22(12):1085–1094.

1006 Orr HA. The population genetics of speciation: the evolution of hybrid incompatibilities. Genetics.
1007 1995;139(4):1805–1813.

1008 Ortiz-Barrientos D, Engelstädter J, Rieseberg LH. Recombination rate evolution and the origin of species.
1009 Trends in ecology & evolution. 2016;31(3):226–236.

1010 Patton EE, Mitchell DL, Nairn RS. Genetic and environmental melanoma models in fish. Pigment cell &
1011 melanoma research. 2010;23(3):314–337.

1012 Penãlba JV, Wolf JB. From molecules to populations: appreciating and estimating recombination rate
1013 variation. Nature Reviews Genetics. 2020;21(8):476–492.

1014 Pool JE. The mosaic ancestry of the Drosophila genetic reference panel and the D. melanogaster reference
1015 genome reveals a network of epistatic fitness interactions. Molecular biology and evolution.
1016 2015;32(12):3236–3251.

1017 Powell DL, García-Olazábal M, Keegan M, Reilly P, Du K, Díaz-Loyo AP, et al. Natural hybridization
1018 reveals incompatible alleles that cause melanoma in swordtail fish. Science. 2020;368(6492):731–736.

1019 Presgraves DC. The molecular evolutionary basis of species formation. Nature Reviews Genetics.
1020 2010;11(3):175–180.

1021 Satokangas I, Martin S, HelanteräH, Saramäki J, Kulmuni J. Multi-locus interactions and the build-up of
1022 reproductive isolation. Philosophical Transactions of the Royal Society B. 2020;375(1806):20190543.

1023 Schartl M, Walter RB, Shen Y, Garcia T, Catchen J, Amores A, et al. The genome of the platyfish,
1024 Xiphophorus maculatus, provides insights into evolutionary adaptation and several complex traits. Nature
1025 genetics. 2013;45(5):567–572.

1026 Schumer M, Brandvain Y. Determining epistatic selection in admixed populations. Molecular Ecology.
1027 2016;25(11):2577–2591.

1028 Schumer M, Cui R, Powell DL, Dresner R, Rosenthal GG, Andolfatto P. High-resolution mapping reveals
1029 hundreds of genetic incompatibilities in hybridizing fish species. Elife. 2014;3: e02535.

1030 Schumer M, Powell DL, Corbett-Detig R. Versatile simulations of admixture and accurate local ancestry
1031 inference with mixnmatch and ancestryinfer. Molecular ecology resources. 2020;20(4):1141–1151.

1032 Schumer M, Powell DL, Delclós PJ, Squire M, Cui R, Andolfatto P, et al. Assortative mating and
1033 persistent reproductive isolation in hybrids. Proceedings of the National Academy of Sciences.
1034 2017;114(41):10936–10941.

1035 Schumer M, Xu C, Powell DL, Durvasula A, Skov L, Holland C, et al. Natural selection interacts with
1036 recombination to shape the evolution of hybrid genomes. Science. 2018;360(6389):656–660.

1037 Seehausen O. Hybridization and adaptive radiation. Trends in ecology & evolution. 2004 ; 19(4) :198–
1038 207.

1039 Simon M, Loudet O, Durand S, Bérard A, Brunel D, Sennesal FX, et al. Quantitative trait loci mapping in
1040 five new large recombinant inbred line populations of Arabidopsis thaliana genotyped with consensus
1041 single-nucleotide polymorphism markers. Genetics. 2008;178(4):2253–2264.

1042 Slatkin M. Linkage disequilibrium—understanding the evolutionary past and mapping the medical future.
1043 Nature Reviews Genetics. 2008;9(6):477–485.

1044 Smith JM, Smith NH, O'Rourke M, Spratt BG. How clonal are bacteria? Proceedings of the National
1045 Academy of Sciences. 1993;90(10):4384–4388.

1046 Smukowski C, Noor M. Recombination rate variation in closely related species. Heredity.
1047 2011;107(6):496–508.

1048 Sved J. The stability of linked systems of loci with a small population size. Genetics. 1968;59(4):543.

1049 Szabo Q, Bantignies F, Cavalli G. Principles of genome folding into topologically associating domains.
1050 Science advances. 2019;5(4): eaaw1668.

Tang S, Presgraves DC. Lineage-specific evolution of the complex Nup160 hybrid incompatibility between Drosophila melanogaster and its sister species. Genetics. 2015;200(4):1245–1254.

Turelli M, Orr HA. Dominance, epistasis and the genetics of postzygotic isolation. Genetics. 2000;154(4):1663–1679.

Turner LM, Harr B. Genome-wide mapping in a house mouse hybrid zone reveals hybrid sterility loci and Dobzhansky-Muller interactions. Elife. 2014;3: e02504.

Turner LM, White MA, Tautz D, Payseur BA. Genomic networks of hybrid sterility. PLoS Genet. 2014;10(2): e1004162.

Wu CI, Palopoli MF. Genetics of postmating reproductive isolation in animals. Annual review of genetics. 1994;28(1):283–308.

Wu CI, Ting CT. Genes and speciation. Nature Reviews Genetics. 2004;5(2):114–122.

Supporting Information

Figure S1. Illustration of the genomic composition and the fitnesses in the haploid model. A. In our toy model of hybridization with a single DMI pair, two recombinant haplotypes (*ab* and *AB*) are generated from the parental haplotypes (*Ab* and *aB*) from the F2 onwards. In the following generations, all four haplotypes are segregating. In the Dobzhansky-Muller incompatibility (DMI) model, the recombinant haplotype *AB* is strongly selected against. Throughout the paper we allow for weak direct selection for the derived alleles (here, $\alpha = 0.001$ for *A* and $\beta = 0.002$ for *B*) and an intermediate to strong fitness interaction between *A* and *B* (here, $\gamma = -0.5$). B. Recombinant imbalance caused by a DMI as compared with Hill-Robertson interference (HRI). Alleles *A* and *B* under strong selection in the same direction can lead to recombinant imbalance between *ab* and *AB*. The arrows show the intensity of the absolute reduction of each haplotype frequency in one generation.

Figure S2. Deterministic frequency dynamics of the four haplotypes in a new hybrid population in the deterministic haploid model. Alleles *A* and *B* are under weak direct selection ($\alpha = 0.001$ for *A* and $\beta = 0.002$ for *B*). The epistatic interaction between alleles *A* and *B* is γ. The recombination probability *c* is 0.1. The admixture proportion is 0.5. A. The haplotype frequencies approach linkage equilibrium soon after hybridization without a DMI ($\gamma = 0$). B. With a strong DMI ($\gamma = -0.5$) the emerging recombinant haplotype *AB* is eliminated quickly, whereas the *ab* haplotype has a marginal advantage that drives it to high frequencies.

Figure S3. Haplotype frequencies that create negative $X(2)$. The three panels represent three different admixture proportions for *Ab* and *aB*. The frequencies of four haplotypes (f_{aB}, f_{Ab}, f_{ab}, f_{AB}) were plotted. Haplotype frequency of *ab* (f_{ab}) is shown on the x axis and the frequencies of other three haplotypes are shown on the y axis. The ratio of f_{aB} and f_{Ab} stays the same as their initial ratio for every combination of haplotype frequencies (f_{aB}, f_{Ab}, f_{ab}, f_{AB}). Haplotype *ab* has always the largest frequency and *AB* has always the smallest frequency.

Figure S4. Dynamics of $D2_{ik}$ and $X(2)$. A-D. $D2_{ik}$ in four scenarios combining equal/unequal admixture proportions and with/without DMIs, obtained from the deterministic haploid model. E-F. $X(2)$ trajectory with (blue dashed line) and without (red line) DMIs. The direct selection coefficients are α= 0.001, β = 0.002. The strength of epistasis is γ = -0.5 (strong DMI) and γ = 0 (no DMI). The recombination probability is 0.1.

Figure S5. Comparison of the dynamics of $X(2)$ and $\Delta D2 = D2_{ab} - D2_{AB}$ for a DMI (A&B) compared with strong direct selection (Hill-Roberson interference, HRI, C&D) in the deterministic haploid model. The direct selection coefficients acting on *A* and *B* are α, β. The admixture proportion is $f = 0.5$. Black dots highlight the generation with the largest $-X(2)$ or $-\Delta D2$ for each trajectory. The values of $X(2)$ and $\Delta D2$ are represented by blue color intensity. Blank areas represent either $X(2)$>0 (to the left of the blue area) or at least one locus close to fixation (minor allele frequency <0.005, on the right of the blue area). The recombination probability between the two DMI loci is 0.1. A&B. DMIs ($\alpha = 0.001,\ \beta = 0.002,\ \gamma < 0$ varies on the y axis) exist for a longer longer time in the population than HRI (C&D). C&D. HRI ($\gamma = 0,\ \alpha\&\beta < 0$, y axis) can briefly induce weak negative $X(2)$ and $\Delta D2_{ik}$ earlier than a DMI, but the two-locus polymorphism is quickly purged from the population.

Figure S6. Negative $X(2)$ pinpoints an intrachromosomal DMI in simulated data. The distribution of $X(2)$, D', and $\Delta D2$ of a chromosome with a DMI pair at generation 50 under a Wright-Fisher model for one simulation run using SLiM. The direct selection coefficients are $\alpha = 0.001, \beta = 0.002$. The strength of epistasis is $\gamma = -0.5$. The interacting loci generating the DMI were located at chromosome 1 (chr1):15 cM and chr2: 15 cM, such that the recombination probability was $c = 0.5$ between the two loci. A-C. Heatmaps of D', $X(2)$ and the $\Delta D2$ within the simulated chromosome at generation 20 (G20). D-F. Heatmaps of D', $X(2)$ and the $\Delta D2$ within the simulated chromosome at generation 50 (G50). Only the DMI loci and their 10 cM flanking regions were shown in D-F. Black arrows highlight the location of the DMI.

Figure S7. Negative X(2) dynamics a DMI persist for long times if there is ongoing immigration from both parental populations. Each line is one simulation run using SLiM, assuming a strong DMI ($\alpha = 0.001, \beta = 0.002,\ \gamma = -0.5$) under a Wright-Fisher model. The recombination probability between the interacting loci was 0.1. 300 individuals were sampled in each simulation. Trajectories were plotted from generation 2 onwards. DMIs can be maintained by symmetric migration from two parental populations ($m1,\ m2 = 0.01$) for a long time, and not affected by the initial admixture proportions (Admix. Pro.).

Figure S8. Proportion of hybrid individuals under five demographic scenarios. Here, hybrids are defined as individuals that derived at least 10% of their genome from each parental population. Each line is one simulation run using SLiM, assuming equal admixture proportions of the parental populations and a strong DMI ($\alpha = 0.001, \beta = 0.002,\ \gamma = -0.5$) under a Wright-Fisher model. The recombination probability between the interacting loci was 0.1. Three hundred individuals were sampled in each simulation.

Figure S9. Dynamics of haplotype frequencies and $X(2)$ for a DMI under diploid Wright-Fisher (WF; dash-dotted line) and Moran (solid line) models for one simulation run using SLiM, assuming a population size of 5000. The model parameters were $\alpha = 0.001,\ \beta = 0.002,\ \gamma = -0.5$, with recombination probability $c = 0.1$ between the DMI loci. Three hundred individuals were sampled in

each simulation. A. Negative $X(2)$ appears ~50 generations earlier under a Wright-Fisher model than under a Moran model. B. Haplotype frequencies change more quickly in the Wright-Fisher model than that in the Moran model. Lines indicate the haplotype frequencies of *AB* (red), *ab* (black), *Ab* (blue) and *aB* (green).

Figure S10. Sensitivity and specificity of negative $X(2)$ for detecting a DMI, computed from 100 simulations of each parameter combination using SLiM, assuming a Wright-Fisher population of 5000 individuals. We considered two admixture proportions, $f = 0.5$ and $f = 0.3$, and three migration rates: 0, 0.01, and 0.05. A strong DMI ($\alpha = 0.001, \beta = 0.002,\ \gamma = -0.5$) and no DMI ($\alpha = 0.001,\ \beta = 0.002,\ \gamma = 0$) were simulated under a Wright-Fisher model. The recombination probability between the DMI loci was $c = 0.1$, and the population size was 5000. Here, any interaction with $X(2) < -0.005$ & $D' < 0$ was taken as a putative DMI. Trajectories ended when one of the interacting loci became monomorphic (indicated by large plot markers). 300 individuals were sampled in each simulation. Vertical lines indicate the 95% confidence interval (Wald method). A&B Sensitivity and specificity using phased data. C & D. Sensitivity and specificity when only homozygous genotypes were used at each locus. A&C. Sensitivity is high unless strong migration leads to swamping of the DMI alleles. B&D. Specificity is high under all tested scenarios. Vertical lines are 95% confidence interval (Wald test).

Figure S11. Sensitivity and specificity of the G test that indicates DMIs ($p < 0.05$). We considered two admixture proportions, $f = 0.5$ and $f = 0.3$, and three migration rates: 0, 0.005, and 0.01. A strong DMI ($\alpha = 0.001, \beta = 0.002,\ \gamma = -0.5$) and no DMI ($\alpha = 0.001, \beta = 0.002,\ \gamma = 0$) were simulated under a diploid Wright-Fisher model. The recombination probability was 0.5. For each parameter combination, we ran 100 simulations with SLiM. Sensitivity (A) was the proportion of successful DMI detections with the strong DMI. Specificity (B) was the proportion of true negative detections without DMI. Trajectories ended when one of the interacting loci became monomorphic or at generation 150 (indicated by large markers). Vertical lines are 95% confidence interval (Wald test).

Figure S12. The distribution of $X(2)$ plotted against p values from the G test. Data were obtained from 100 simulations of a single DMI under a diploid Wright-Fisher model. Here, we used the same data as in Figure 5 and S11 with equal admixture proportions and no migration within 150 generations, i.e., the data points represent the $X(2)$ and G test statistics at the DMI loci, pooled across all sampling points. A strong DMI ($\alpha = 0.001, \beta = 0.002,\ \gamma = -0.5$) was simulated under a diploid Wright-Fisher model. The recombination probability was 0.5. The distribution was zoomed into two areas by two independent criteria for detecting DMI: (A) small p values by G test ($p < 0.05$); (B) negative $X(2)$ values. Red dots indicate DMIs that are observed before Generation 5 with a significant p value by the G test in panel A. Black dots indicate DMIs after Generation 5 in panel A and B. Only 9.9% of the simulations showed a significant p value by the G test ($p < 0.05$) in panel B.

Figure S13. Sensitivity and specificity of negative $X(2)$ (A&B) and G test (C&D) indicating DMIs when only homozygous genotypes were used at each locus. We considered two admixture proportions, $f = 0.5$ and $f = 0.3$ and three migration rates (m): 0, 0.005 and 0.01. A strong DMI ($\alpha = 0.001, \beta = 0.002,\ \gamma = -0.5$) for sensitivity and no DMI ($\alpha = 0.001, \beta = 0.002,\ \gamma = 0$) for specificity were simulated under a diploid Wright-Fisher model. The recombination probability was 0.5. For each parameter combination, we ran 100 simulations using SLiM. In panel A&B, any interaction with $X(2) <$

-0.005 & $D' < 0$ was taken as a putative DMI. In panel C&D, any interaction with p<0.05 was taken as a putative DMI. Sensitivity (A&C) was the proportion of successful DMI detections with the strong DMI. Specificity (B&D) was the proportion of true negative detections without DMI. Trajectories end when one of the interacting loci became monomorphic or at generation 150 (indicated by large markers). Vertical lines are 95% confidence interval (Wald test).

Figure S14. Distributions of negative $X(2)$ when $D' < 0$ for DMI detection under four demographic scenarios. This figure represents two starting frequencies of the minor parental population, $f = 0.5$ and $f = 0.3$, and different immigration rates from the two parental populations ($m1$ from minor parental population, $m2$ from major parental population). Light green boxes show the $X(2)$ distribution for the three-locus two-DMI model (3-locus) and the other boxes for the four-locus two-DMI model. DMIs are randomly distributed on four chromosomes. Direct selection coefficients on two incompatible alleles were drawn from an exponential distribution with mean = 0.001. Epistatic coefficients were drawn from a uniform distribution [-1, -0.001). We calculated $X(2)$ statistics using homozygous genotypes from a sample of two hundred individuals for each simulation. We simulated each scenario for 100 times with SLiM. $X(2)$ values were summarized for three types of genomic regions, neutral chromosomes (A), chromosomes with DMIs (B), and individual DMI loci (C). Boxplots represent the interquartile range; whiskers extend to minimal and maximal values. The dash line is $X(2) = -0.005$.

Figure S15. Propagation of the DMI signal into flanking regions in simulated data (sampled at generation 30, significance threshold: X(2)<-0.005 & D'<0) when only homozygous genotypes were sampled (sampling criteria for panels A&B: homozygous genotype frequency >0.05, heterozygosity<0.6; panel C shows homozygous data without further filtering). Data resulted from 100 simulations using SLiM, in which two DMIs (i.e., four DMI loci) were randomly distributed on four chromosomes, thus resulting in inter- and intrachromosomal DMIs. The direct selection coefficients α and β were drawn from exponential distribution with mean value 0.001. The strength of epistasis was drawn from a uniform distribution, γ∈[-1, -0.001], which is represented by the blue color intensity in panels B&C. To resemble the demography of the studied hybrid swordtail fish populations, the admixture proportion was set to f=0.3 and the migration rate was m=0.01. 200 individuals were sampled from each simulation to obtain the statistics. A. The number of significant marker pairs decreases rapidly with distance to the nearest true DMI locus. B&C. Proportion of significant marker pairs when statistics were computed for all pairs between two increasingly large regions around the true interacting DMI loci, with (B) and without (C) strict sampling criteria. Red dots indicate the median obtained from 100 simulations.

Figure S16. The observed occurrence spectra of detected DMI candidates in the hybrid populations is skewed towards low and high frequencies compared to the expected distribution. The bar plot shows the frequency of occurrence of loci in the putative DMIs for each population. The blue line shows the expected occurrence distribution under a Poisson distribution.

Figure S17. Chromosomal illustration of putative DMIs in three hybrid populations (CHAF, TLMC and TOTO). Some loci have many putative interacting partners. Each line is colored by the number of putative partners of the two involved candidate loci. In TOTO, loci show a smaller number of interactions than in CHAF and TLMC.

Figure S18. Example of an intrachromosomal DMI candidate in hybrid swordtail fish on chromosome 20. The values of $X(2)$, linkage disequilibrium (D'), and recombinant imbalance ($\Delta D2 = D2_{MB} - D2_{BM}$) are

presented by color intensity. As highlighted by an arrow, the candidate DMI was detected in TLMC between locus chr20:9Mb (B alleles) and chr20:10Mb (M alleles). In CHAF, the residual parental linkage is still so strong that $X(2)$ >0, but $\Delta D2$ shows a weak recombinant imbalance. In TOTO, a stronger interaction presumably happened between chr20:8Mb and chr20:11Mb such that we see no significant signal between locus chr20:9Mb and chr20:10Mb.

Figure S19. Example of an interchromosomal DMI candidate in hybrid swordtail fish between chromosome 19 and 20. The values of $X(2)$, linkage disequilibrium (D') and recombinant imbalance (Recomb. $\Delta D2 = D2_{MB} - D2_{BM}$) are presented by color intensity. As highlighted by an arrow, the candidate DMI was inferred in TLMC between locus chr19:8-9Mb (B alleles) and chr20:23Mb (M alleles). We suspect that negative $X(2)$ is due to linkage and that the true DMI locus has been fixed in all three populations. Most of the homozygous M alleles at chr20:22-24Mb have been purged in TOTO but not at chr19:8-9Mb. CHAF shows a larger genomic region involved in DMI than TLMC, which might be due to the recombination map at the first several generations after hybridization.

Figure S20. Scatterplot of $X(2)$ and D' for markers occurring at *Xmrk* and its interacting locus *cdkn2a/b*. Markers were extracted from the focal genes and their flanking regions (*cdkn2a/b at* chr5:15.7Mb-16Mb*, Xmrk* at chr21:16.5Mb-17.5Mb). No pairs of markers in TLMC passed the filtering criteria. A large proportion of pairs are $D' < 0$ & $X(2) < 0$ in both CHAF and TOTO between *Xmrk* and *cdkn2a/b.* Negative $X(2)$ values are larger in TOTO (age, ~35 generations) than in CHAF (age, ~25 generations). In TOTO, $D' = -1$ & $X(2) < 0$ indicates the absence of genotypes that are linked to DMIs, possibly due to sampling at low frequencies or completed purging of incompatible alleles. Colouring indicates point density.

Figure S21. Dominance effects on $X(2)$ dynamics of DMIs. The four DMI scenarios are a DMI in the haploid model, homozygous-homozygous DMI (h0<<h1), homozygous-heterozygous DMI (recessive), and heterozygous-heterozygous DMI (codominant). All trajectories were generated with the same parameters. Incompatible alleles *A* and *B* are under weak direct selection ($\alpha = 0.001$ for *A* and $\beta = 0.002$ for *B*). The strength of the epistatic interaction between alleles *A* and *B*, γ, is -0.5. The recombination probability *c* is 0.1. The admixture proportion is 0.5.

Figure S22. The number of two-locus homozygous-homozygous haplotypes for different sampling sizes ($n = 100,\ 200,\ 300$), obtained from a set of 100 simulations for each parameter combination using SLiM. Simulations were performed assuming a diploid Wright-Fisher population with 5000 individuals. In each simulation, two DMIs were randomly distributed on four chromosomes (Chr w DMI). Two additional neutral chromosomes (Chr w/o DMI) were also simulated in the same genome. The number of two-locus homozygous-homozygous haplotypes for each pair loci were counted at generation 30 and 50 (G30 & G50). Neutral chromosomes contain fewer two-locus homozygous-homozygous haplotypes on average than chromosomes with DMIs. Boxes represent the interquartile range, and whiskers extend to 95% confidence interval.

Table S1. False positive rate under three filtering criteria in simulations of a single DMI

Table S2. False positive rate under three filtering criteria in simulations of two DMIs

1247 Table S3. False positive rate under three filtering criteria simulations of two DMIs when only
1248 homozygous loci are used for analyses

1249 Table S4. Characteristics of the three hybrid swordtail fish populations and the corresponding genomic
1250 data

1251 Table S5. Bootstrapping statistics to define putative DMI in the three hybrid populations

1252 Table S6. 1Mb bins involved in >10 negative interactions

1253 Table S7. DMIs supported by >1 hybrid populations

1254 Table S8. Single interacting bins shared by all three populations

1255 Table S9. Summary of $X(2)$ values between *Xmrk* and its interacting genes, *cd97* and *cdkn2a/b*

1256 Table S10. The number of heterozygous loci in a pair of haplotypes

1257 Table 11. Selection forces (epistasis and direct selection) and dominance at a DMI. Each field in the table
1258 indicates the fitness of the corresponding genotype

1259 Table S12. Parameterization of the two- and three-locus DMI models